

2

AD-A266 257



PL-TR-93-2087

**RESEARCH IN REGIONAL SEISMOLOGY:
THE EFFECT OF ANISOTROPY**

Batakrishna Mandal
M. Nafi Toksöz
William Rodi

Earth Resources Laboratory
Department of Earth, Atmospheric, and
Planetary Sciences
Massachusetts Institute of Technology
Cambridge, MA 02139

1 March 1993

Final Report
1 October 1991— 27 September 1992

APPROVED FOR PUBLIC RELEASE; DISTRIBUTION UNLIMITED

DTIC
ELECTE
JUL 01 1993
S E D



PHILLIPS LABORATORY
Directorate of Geophysics
AIR FORCE MATERIEL COMMAND
HANSCOM AIR FORCE BASE, MA 01731-3010

422715

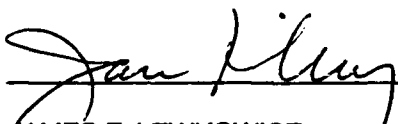
93-14818



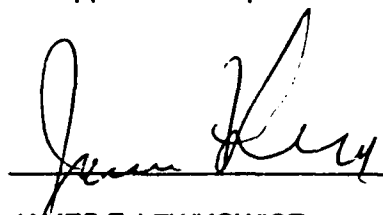
93 6 29 070

The views and conclusions contained in this document are those of the authors and should not be interpreted as representing the official policies, either expressed or implied, of the Air Force or the U.S. Government.

This technical report has been reviewed and is approved for publication.



JAMES F. LEWKOWICZ
Contract Manager
Solid Earth Geophysics Branch
Earth Sciences Division



JAMES F. LEWKOWICZ
Branch Chief
Solid Earth Geophysics Branch
Earth Sciences Division



DONALD H. ECKHARDT, Director
Earth Sciences Division

This document has been reviewed by the ESD Public Affairs Office (PA) and is releasable to the National Technical Information Service (NTIS).

Qualified requestors may obtain additional copies from the Defense Technical Information Center. All others should apply to the National Technical Information Service.

If your address has changed, or if you wish to be removed from the mailing list, or if the addressee is no longer employed by your organization, please notify PL/TSI, Hanscom AFB MA 01731-3010. This will assist us in maintaining a current mailing list.

Do not return copies of this report unless contractual obligations or notices on a specific document requires that it be returned.

REPORT DOCUMENTATION PAGE			Form Approved OMB No 0704-0188	
Public reporting burden for this collection of information is estimated to average 1 hour per response, including the time for reviewing instructions, searching existing data sources, gathering and maintaining the data needed, and completing and reviewing the collection of information, and comments regarding this burden estimate or any other aspect of this collection of information, including suggestions for reducing this burden, to Washington Headquarters Services, Directorate for Information Operations and Reports, 1215 Jefferson Davis Highway, Suite 1204, Arlington, VA 22202-4302, and to the Office of Management and Budget, Paperwork Reduction Project (0704-0188), Washington, DC 20503				
1. AGENCY USE ONLY (Leave blank)	2. REPORT DATE 1 March 1993	3. REPORT TYPE AND DATES COVERED Final Technical 10/1/91-9/27/92		
4. TITLE AND SUBTITLE Research in Regional Seismology: The Effect of Anisotropy			5. FUNDING NUMBERS F19628-90-K-0057 PE 62101F PR 7600 TA 09 WU AY	
6. AUTHOR(S) Batakrishna Mandal M. Nafi Toksöz William Rodi				
7. PERFORMING ORGANIZATION NAME(S) AND ADDRESS(ES) Earth Resources Laboratory Dept. of Earth, Atmospheric, and Planetary Sciences Massachusetts Institute of Technology 77 Massachusetts Avenue Cambridge, MA 02139			8. PERFORMING ORGANIZATION REPORT NUMBER 74527	
9. SPONSORING/MONITORING AGENCY NAME(S) AND ADDRESS(ES) Phillips Laboratory 29 Randolph Road Hanscom AFB, MA 01731-3010 Contract Manager: James Lewkowicz/GEPH			10. SPONSORING/MONITORING AGENCY REPORT NUMBER PL-TR-93-2087	
11. SUPPLEMENTARY NOTES				
12a. DISTRIBUTION / AVAILABILITY STATEMENT Approved for Public Release: Distribution Unlimited			12b. DISTRIBUTION CODE	
13. ABSTRACT (Maximum 200 words) The objective of this study is to quantify the effects of fracturing and anisotropy in the vicinity of an underground explosion on the resulting seismic radiation patterns and in particular on the generation of shear waves. Theoretical finite difference calculations show that an explosive source embedded in either an anisotropic or randomly heterogeneous medium generates shear waves, with anisotropy at the source inducing larger shear waves than heterogeneity. We review existing theories of the effective elastic moduli of micro-fractured and macro-fractured rocks to determine realistic models of anisotropic source media.				
14. SUBJECT TERMS Anisotropy; fractures; scattering			15. NUMBER OF PAGES 70	
			16. PRICE CODE	
17. SECURITY CLASSIFICATION OF REPORT UNCLASSIFIED	18. SECURITY CLASSIFICATION OF THIS PAGE UNCLASSIFIED	19. SECURITY CLASSIFICATION OF ABSTRACT UNCLASSIFIED	20. LIMITATION OF ABSTRACT SAR	

TABLE OF CONTENTS

List of Contributing Scientists	iv
List of Previous and Related Contracts	iv
Bibliography of Publications Totally or Partially Supported by the Contract	iv
Preface	v
Radiation Patterns From Explosions in Anisotropic and Heterogeneous Media ...	vii
Summary	vii
Introduction	1
Finite Difference Algorithm in Anisotropic and Heterogeneous Media	3
Radiation Patterns	5
Conclusions	11
References	12
Figures	16
Scale of Anisotropy: A Theoretical Study of Velocity Anisotropy for Micro- and Macro-Fractures	31
Summary	31
Introduction	32
Micro-Fracture Model	33
Hudson Model	34
Macro-Fracture Model	38
Discussion	42
References	43
Figures	44

List of Contributing Scientists

Batakrishna Mandal, Research Scientist, Massachusetts Institute of Technology

M. Nafi Toksöz, Professor of Geophysics, Massachusetts Institute of Technology

William Rodi, Postdoctoral Associate, Massachusetts Institute of Technology

List of Previous and Related Contracts

DARPA/GL Contract F19628-88-K-0036 "Seismic Wave Propagation, Attenuation and Scattering over Regional Distances", August 1988 to July 1989.

DARPA/AFGL Contract F19628-89-K-0020 "Regional Seismograms: Attenuation and Scattering", July 1989 to June 1991.

Bibliography of Publications Totally or Partially Sponsored by the Contract

Gibson, Jr., R.L., and M.N. Toksöz, 1991. Ray-Born synthetic seismograms for 3-D, anisotropic and inhomogeneous media: applications to fracture zones. *Submitted to Geophys. J. Int.*

Toksöz, M.N., B. Mandal, R.L. Gibson Jr., and A.M. Dainty, 1991. Research in regional seismology: the effect of anisotropy. *Papers Presented at 13th Ann. PL/DARPA Seismic Res. Symp.*, 445-452. PL-TR-91-2208, ADA241325

PREFACE

The objective of this study is to quantify the effects of fracturing and anisotropy in the vicinity of an underground explosion on the resulting seismic radiation patterns and in particular on the generation of shear waves. In previous work under this contract we applied wavenumber integration and ray-Born modeling techniques to address this problem. The present study employs finite difference modeling to compare the effects of anisotropy near the source with the effects of random heterogeneity and the combined effects of anisotropy and heterogeneity. The results show that the source radiation pattern does greatly depend on the medium properties in the source region, and that an explosive source in an anisotropic medium generates larger shear waves than an explosion in a randomly heterogeneous medium of similar contrast in parameters. In addition, we review the existing theories of the effective elastic moduli of micro-fractured and macro-fractured media. We discuss the limitations of these theories and study their implications for the difference between the shear wave velocity variations of micro- and macro-fractured media.

DTIC QUALITY INSPECTED 5

Accession For	
NTIS CRA&I	<input checked="" type="checkbox"/>
DTIC TAB	<input type="checkbox"/>
Unannounced	<input type="checkbox"/>
Justification	
By	
Distribution/	
Availability Codes	
Dist	Avail and/or Special
A-1	

RADIATION PATTERNS FROM EXPLOSIONS IN ANISOTROPIC AND HETEROGENEOUS MEDIA

Summary

The generation of shear waves from an explosive source in a complex medium (including anisotropy and heterogeneity) has been investigated using theoretical calculations of seismograms and radiation patterns. We developed a cylindrical coordinate finite difference algorithm for anisotropic/heterogeneous media to perform these calculations. The algorithm was applied to models composed of various combinations of anisotropy and random heterogeneity, including some where the source and propagation media were different. In agreement with a similar study of the generation of shear waves from explosions (Mandal and Toksöz, 1990), we find that shear wave generation in two physical types of anisotropic media (media with micro-fractures and macro-fractures or joints) have different properties. We also find that an explosive source in an anisotropic medium of either type generates larger amplitude shear waves than an explosive source in a randomly heterogeneous medium of similar contrast in parameters. Finally, we find that the source radiation pattern is controlled primarily by the medium properties at the source region.

Introduction

Extensive studies have been done to understand the generation of transverse motion from underground nuclear explosions (e.g., Kisslinger *et al.*, 1961; Press and Archambeau, 1962; Toksöz *et al.*, 1964; Archambeau and Sammis, 1970; Toksöz and Kehrler, 1972; Massé, 1981; Wallace *et al.*, 1983, 1985; Gupta and Blandford, 1983; Johnson, 1988; Lynnes and Lay, 1988; Priestley *et al.*, 1990; Mandal and Toksöz, 1990, 1991). From these studies various mechanisms have been proposed, among which are tectonic strain release by relaxation of the medium around the explosion-generated cavity, triggering of an earthquake, dislocation across cracks, spallation and "slapdown," anisotropy in the source medium, and scattering from heterogeneities near the source. It has been concluded that no single mechanism explains all of the data (Massé, 1981; Gupta and Blandford, 1983; Johnson, 1988).

The complexity of the explosion-source phenomenon in a variety of media, including heterogeneous, anisotropic and pre-stressed media, was reviewed by Patton and Taylor (1991). They found that the physical structure beneath nuclear test sites is complex and cannot be modeled as simple (e.g., isotropic and layered) media. Several observational studies have shown that most crustal rocks have some degree of seismic anisotropy (e.g. Stephen, 1981, 1985; Crampin, 1984; Lo *et al.*, 1986; Thomsen, 1986; Winterstein, 1986; Martin, 1990) as well as some degree of heterogeneity (e.g., Cassell and Fuchs, 1979; Taylor, 1983; Kennett and Bowman, 1990; Kennett and Nolet, 1990). Seismic anisotropy can be caused by several mechanisms, such as: (1) preferred orientation of the minerals due to deposition or

metamorphism; (2) geometric effects, such as alternating high- and low-velocity thin beds (e.g., shales, carbonates); (3) preferred orientation of micro- and macro-fractures in the shallow crust; and (4) the presence of local or regional tectonic stress. Moreover, evidence of anisotropy and small-scale heterogeneity are commonly found in subsurface core data. The prevalence of anisotropy and heterogeneity in crustal rocks motivates the present study.

Our study examines the influence of anisotropy and heterogeneity at and near the source on the seismic radiation from explosions. A question of primary concern is the relative importance of various medium properties as generators of shear wave radiation from explosive sources, a question which bears greatly on the problem of discriminating explosions from earthquakes on the basis of seismic observations. To address this question we model the source radiation patterns of P and S waves for explosions set off in various complex media which include anisotropy, small-scale heterogeneity, and mixtures of both. In addition, we consider media which have different properties in the region of the source compared to the remainder of the propagation path. Thus, many types of medium complexity are considered.

The present study extends earlier studies by the authors of near-source anisotropy (Mandal and Toksöz, 1990, 1991). The earlier studies examined the effects of anisotropy in the absence of heterogeneity using analytical synthetic seismogram techniques for layered earth models (i.e., wavenumber integration). Such techniques are unable to handle the more complex media addressed in the present study. For this purpose we have developed a finite difference algorithm for anisotropic and heterogeneous media.

Finite Difference Algorithm in Anisotropic and Heterogeneous Media

We developed a finite difference algorithm to study the source radiation pattern in anisotropic and heterogeneous media. When considering a point source radiation pattern, we use a cylindrical coordinate system. The two-dimensional cylindrical coordinate finite difference algorithm limits the anisotropic medium to an azimuthally symmetric medium. This algorithm is the discretized form of the first-order velocity-stress formulation of the wave equation on a staggered grid (e.g., Virieux, 1986; Levander, 1988). This staggered grid formulation is known to exhibit smaller grid dispersion and grid anisotropy than centered grid finite difference algorithms. The basic first-order partial differential formulations for anisotropic media with a vertical axis of symmetry are given by the wave equations:

$$\rho \partial_t v_r = f_r + \partial_r \sigma_{rr} + \partial_z \sigma_{rz}$$

$$\rho \partial_t v_z = f_z + \partial_z \sigma_{zz} + \partial_r \sigma_{rz}$$

and the time derivatives of the stress-strain relations:

$$\partial_t \sigma_{rr} = c_{11} \partial_r v_r + c_{13} \partial_z v_z$$

$$\partial_t \sigma_{zz} = c_{13} \partial_r v_r + c_{33} \partial_z v_z$$

$$\partial_t \sigma_{\theta\theta} = c_{12} \partial_r v_r + c_{13} \partial_z v_z$$

$$\partial_t \sigma_{rz} = c_{44} (\partial_z v_r + \partial_r v_z)$$

where v_i are velocities, f_i are body forces, σ_{ij} are stresses, ρ is density, and c_{ij} are the elastic constants. We consider the r and z axes as the symmetry axes. Simple sponge absorption layers are used at the bottom and left boundary of the grid to avoid unwanted reflections at the boundary. The proper discretization in space and time has also been considered to minimize the well-known dispersion problem for finite difference computation. In this case, ten points per wavelength grid size with fourth order finite difference in space and second-order in time scheme sufficiently minimizes the grid dispersion and grid anisotropy problem.

To minimize the numerical error of the finite difference method, we need huge computational power along with computer storage to compute even a simple physical model. This is the main drawback of the finite difference method. Recent advances in the technology of parallel processing allow us to overcome this problem. The parallel processors not only speed up the computational time, but have also a large memory for a physical model for the theoretical study of wave propagation. While finite difference algorithms are fundamentally parallel in nature, their proper implementation on a parallel computer is necessary and must be tailored to the particular architecture and hardware limitations of the target machine.

There are a variety of parallel computers. The critical characteristics to consider are the number of individual processors, the connectivity and communication mechanism between processors, the control scheme for running the processors, and the amount of memory accessible by each processor. Among the various types of parallel computers available today, the

MIMD (Multiple Instruction Multiple Data) architecture computer is highly suitable to a variety of problems, including finite difference problems. We implemented our finite difference algorithm on one such machine, the nCUBE-2. The parallel algorithm decomposes the whole finite difference grid into subgrids. Each processor computes the finite difference computations in the subgrid and exchanges information from the edges of the subgrid with adjacent processors to which it is connected. The speed of the computational procedure scales almost inversely with the number of processors. Our implementation on the nCUBE-2 is able to handle the large models needed for practical problems in seismic wave propagation.

Radiation Patterns

In our previous studies (Mandal and Toksöz, 1990, 1991) we showed that the radiation from explosion sources can be affected strongly by the presence of anisotropy, including the generation of shear waves and radiation patterns that mimic double couple sources in isotropic media. Such effects are usually attributed to tectonic release from either triggered faults or relaxation of prestress at the shot point. The velocity anisotropy due to aligned micro- or macro-fractures could be explained in terms of an equivalent medium (e.g., Hudson, 1980, 1981; Schoenberg, 1983; Crampin, 1984; Mandal and Toksöz, 1992).

In the present study we model the propagation effects in media which are more complex. We consider three types of media: (1) homogeneous and anisotropic media; (2) isotropic and randomly heterogeneous media; and (3) media that are both anisotropic and laterally

heterogeneous. Some models are composite media, in which a local region around the source (the "source medium") is of one of the three types while the rest of the medium (the "propagation medium") is of a different type. We studied various media constructed with different types of source and propagation media.

Anisotropic and heterogeneous media are constructed by modifying a simple background, or reference, medium. The background medium we used is a homogeneous, isotropic medium with a P velocity of 6 km/sec, S velocity of 3.46 km/sec and density of 2.6 gm/cc. Anisotropic media are derived by introducing micro-fractures or macro-fractures into this isotropic background. The heterogeneous media are constructed by adding pseudo-random fluctuations in the parameters generated from a specified stationary random process. For composite media (different source and propagation media) we defined the source region to be a sphere of 1 km radius centered on the source.

For each medium constructed, a finite difference calculation was performed with the source taken to be a point dilatation. The source function is bandlimited between 0 and 13 Hz with a 5 Hz center frequency. Synthetic seismograms were computed at two circular arrays in a vertical plane with radial distances of 2 and 4 km, as shown in Figure 1. We display the waveforms in radial (away from source) and tangential (along the θ direction) components. This display explains the transverse motion as well as the radiation pattern from an explosion. To facilitate comparisons between media the seismograms in all figures are plotted on a common scale. As a baseline, Figure 2 shows the waveforms due to an

explosion source in the reference isotropic, homogeneous medium. Since no conversion to shear waves is possible in this medium, the radial component seismograms show the complete dilatation source while the tangential components are zero.

Figure 3 shows the results for an explosive source in a randomly heterogeneous, isotropic medium. The medium is a realization of a stationary random process. The r.m.s. fluctuation in the medium parameters (P and S velocities) is 5% of their background values. The process has an exponential correlation function with the horizontal and vertical correlation length both equal to 0.5 km. Note that random with exponential correlation functions are generally rougher than those with Gaussian correlation functions and smoother than those with Von Karman correlation functions. The results (Figure 3) show the scattering transverse wave in the tangential direction generated from an explosive source. The P-wave velocity is slower than the isotropic medium at 4 km distance.

Figure 4 shows the results for another randomly heterogeneous medium, obtained by letting the correlation lengths in the horizontal and vertical directions differ. That is, the medium is statistically "anisotropic". The horizontal correlation length is 5 km and the vertical is 0.5 km. The correlation function (exponential) and r.m.s. variation (5%) are the same as before. The waveforms in Figure 4 are smoother than those in Figure 3. The heterogeneity with anisotropic characteristics does not produce large shear waves as occur in the next examples.

Figures 5-6 show the waveforms for two different kinds of anisotropic media. Figure 5

shows the results for the medium whose anisotropy owes to uniformly aligned micro-fractures, while in Figure 6 anisotropy is caused by aligned joints. The micro-fracture model is created using second-order Hudson's (1980, 1981) expressions of equivalent elastic constants for aligned penny-shaped fractures with small aspect ratio. In this case, we use 10% fracture density and an aspect ratio of 0.001. The equivalent elastic constants for joints are calculated using the displacement discontinuity model (e.g., Schoenberg, 1983). In this case, we use 100 joints/meter and 15×10^{12} Pa/meter specific stiffness of the joints (the ratio of the incremental stress across the joints to the incremental displacement that the stress produces). These two media are designed to yield a similar P-wave velocity variation. The major distinction between them is the quasi-SV velocity. For a joint medium, the quasi-SV velocity does not have any variation along the anisotropic plane (e.g., Schoenberg, 1983; Mandal and Toksöz, 1992). We see from Figures 5 and 6 that both media produce strong shear waves. The joint medium (Figure 6) produces a radiation pattern similar to a double couple shear wave source. The micro-fracture model (Figure 5) produces a complicated shear wave radiation pattern at the near distance (2 km). The P-wave radiation patterns for the two media are different.

Next, we turn to composite models in which the source medium (within 1 km of the source) and propagation medium (beyond 1 km) are different (see Figure 7). The first three cases consider the mixture of isotropic and anisotropic media. Figure 8 shows the radiation patterns when the propagation medium is the isotropic, homogeneous background and the

source medium is the micro-fractured medium that was used in Figure 5. Comparing Figure 8 to Figure 5, we see that the shear wave radiation pattern at 4 km is noticeably altered by an isotropic propagation medium. For Figure 9, the propagation medium is again the background, but the source medium is now the macro-fractured medium used in the results of Figure 6. In the third case, shown in Figure 10, the source and propagation medium are reversed from Figure 9, i.e., the source medium is the background and the propagation medium is the anisotropic, macro-fractured medium. In this last case, shear waves cannot be produced directly by the source but only by P to S conversion at the source/propagation region interface. Thus the transverse components in Figure 10 are much smaller than the other models using macro-fractured media (Figures 6 and 9).

Figure 11 shows the radiation patterns from a more complex composite model, in which the source medium is anisotropic and the propagation medium is randomly heterogeneous. The anisotropy is of the macro-fracture (joints) type, as used for Figure 6, while the heterogeneity is the same as that used for Figure 3. The results show that significant shear waves are generated and that they are distorted by propagation through the heterogeneous medium. Figure 12 shows the reverse situation from Figure 11, where the source and propagation media are switched. Note that the shear wave amplitude differs distinctly from Figure 11 owing to the fact that anisotropy at the source is a more efficient generator of shear wave energy than heterogeneity at the source.

In the last example, we show a medium that is everywhere (source and propagation

regions) heterogeneous as well as anisotropic. While the entire earth may not be this complex, observations show that the subsurface near faulted regions consists of both aligned fractures and rough spatial variations in elastic properties. We generate a complex model of this type by representing each anisotropic elastic constant as a spatially random field. That is, we use the elastic constants for an aligned joint model for 50 joints/meter with 15×10^{12} Pa/meter specific stiffness as a reference medium, and then add random fluctuations to each elastic constant which are the realization of a random process. The random process we use has the same statistics as the earlier medium of Figure 3, with an r.m.s. variation of 5% and an exponential correlation function with horizontal and vertical correlation lengths of 0.5 km. The waveforms for the resulting medium are shown in Figure 13. Comparing to the results in Figures 3, 6, and 11, we see that the waveforms in this complex medium are dominated by the effect of anisotropy.

All of these numerical examples are shown to determine whether shear wave generation from an explosion source can be explained by various propagation effects near the source. To more easily compare the degree of shear wave generation in various media, we compare their shear to compressional maximum amplitude ratio in Figures 14 and 15. These figures show the S to P amplitude variation as a function of take-off angle from the source at distances of 2 and 4 km from the source. The ratios are shown for the ten models described above, corresponding to Figures 3-6 and 8-13. Note that the models involving anisotropic media (Micro, Joints, Micro_Iso, Joints_Iso, Joints_Hetero-1, Hetero+Joints) produce large S to P

ratios. In some cases, the shear wave energy can be more than 80% of the P-wave. We also see that the shear wave energy depends solely on the source medium type. For example, in all types of heterogeneous media (Hetero-1, Hetero-2, Hetero-1_Joints), the source shows similar magnitudes of S/P ratios. A third observation we can make is that a source in a micro-fracture medium (Micro, Micro_Iso) yields a complicated S/P ratio. This is due to the complicated distribution of shear wave compliances. Finally, we note that the model Iso_Joints, with an isotropic source region and anisotropic propagation medium, produces the smoothest S/P ratio. In this case, the shear waves are generated as a result of conversion at the isotropic and anisotropic interface. At a distance of 4 km the effect is of a similar order to the one observed at 2 km.

Conclusions

Using finite difference modeling, we studied two mechanisms of shear energy generation by explosive sources: anisotropy and random heterogeneity of the medium near the source. Our calculations show that both mechanisms can generate a significant amount of shear waves and transverse motion from an explosion. This is explained by the directional dependence of the compliance in anisotropic and heterogeneous media. We found that anisotropy at the source produces stronger shear waves than heterogeneity, even when the statistical characteristics of the heterogeneity are direction-dependent. We also found that there are two different radiation patterns for the source in the two different anisotropic models (micro- fractures

and macro-fractures/joints). Finally, even when the material closest to the source (with a 1 km radius) is allowed to differ from the material farther away, we find that the characteristics of the medium at/nearer the source primarily determine the degree of shear wave generation.

References

- Archambeau, C.G. and C. Sammis, 1970. Seismic radiation from explosions in prestressed media and the measurement of tectonic stress in the Earth, *Rev. Geophys.*, *6*, 241-288.
- Crampin, S., 1984. Effective elastic constants for wave propagation through cracked solids, *Geophys. J.R. astr. Soc.*, *78*, 691-710.
- Cassell, B. and K. Fuchs, 1979. Seismic investigations of the subcrustal lithosphere beneath Fennoscandia, *J. Geophys.*, *46*, 369-384.
- Gupta, I.N. and R.R. Blandford, 1983. A mechanism for generation of short-period transverse motion from explosions, *Bull. Seism. Soc. Am.*, *73*, 571-591.
- Hudson, J.A., 1980. Overall properties of a cracked solid, *Math. Proc. Camb. Phil. Soc.*, *88*, 371-384.
- Hudson, J.A., 1981. Wave speeds and attenuation of elastic waves in material containing cracks, *Geophys. J. Roy. astr. Soc.*, *64*, 133-150.
- Johnson, L.R., 1988. Source characteristics of two underground nuclear explosions, *Geophys. J.*, *95* 15-30.
- Levander, A. R., 1988. Fourth-order finite-difference P-SV seismograms, *Geophys.*, *53*, 1425-1436.

- Lo, T.W., K.B. Coyner, and M.N. Toksöz, 1986. Experimental determination of elastic anisotropy of Berea sandstone, Chicopee shale and Chelmsford granite, *Geophysics*, 51, 164-171.
- Lynnes, C.S. and T. Lay, 1988. Analysis of amplitude and travel-time anomalies for short-period P-waves from NTS explosions, *Geophys. J.*, 92, 431-443.
- Kennett, B.L.N. and J.R. Bowman, 1990. The velocity structure and heterogeneity of the upper mantle, *Phys. Earth Planet. Inter.*.
- Kennett, B.L.N. and G. Nolet, 1990. The interaction of the S-wavefield with the upper mantle heterogeneities, *Geophys. J. R. astr. Soc.*, 101, 751-762.
- Kisslinger, C., E.J. Mateker, Jr., and T.V. McEvilly, 1961. SH motion from explosions in soil, *J. Geophys. Res.*, 66, 3487-3496.
- Mandal, B., and M.N. Toksöz, 1990. Computation of complete waveforms in general anisotropic media-results from an explosion source in anisotropic medium. *Geophys. J. Int.*, 103, 33-45.
- Mandal, B., and M.N. Toksöz, 1991. Effects of an explosive source in an anisotropic medium, *AGU Monograph "Explosion Source Phenomenology"*, 65, 261-268.
- Mandal, B., and M.N. Toksöz, 1992. Scale of anisotropy: A theoretical study of velocity anisotropy from micro and macro fractures, submitted to *Rev. of Geophysics*.
- Martin, R.M., 1990. Anisotropy of Topopah Spring Member Tuff, New England Research Report.

- Massé, B.P., 1981. Review of seismic source models for underground nuclear explosions, *Bull. Seism. Soc. Am.*, *71*, 1249-1268.
- Patton, H.J. and S.R. Taylor (eds.), 1991. *Explosion Source Phenomenology*, AGU Geophysical Monograph Series, 268p.
- Press, F. and C. Archambeau, 1962. Release of tectonic strain by underground nuclear explosions, *J. Geophys. Res.*, *68*, 5777-5787.
- Priestley, K.F., W.R. Walter, V. Martynov, and M.V. Rozhkov, 1990. Regional seismic recordings of the Soviet nuclear explosion of the joint verification experiment, *Geophys. Res. Lett.*, *17*, 179-182.
- Schoenberg, M., 1983. Reflection of elastic waves from periodically stratified media with interfacial slip. *Geophys. Prospect.*, *31*, 265-292.
- Stephen, R.A., 1981. Seismic anisotropy observed in upper oceanic crust, *Geophys. Res. Lett.*, *8*, 865-868.
- Stephen, R.A., 1985. Seismic anisotropy in the upper oceanic crust, *J. Geophys. Res.*, *90*, 11383-11396.
- Taylor, S.R., 1983. Three-dimensional crust and upper mantle structure at the Nevada Test Site, *J. Geophys. Res.*, *88*, 2220-2232.
- Thomsen, L., 1986. Weak elastic anisotropy, *Geophysics*, *51*, 1954-1966.
- Toksöz, M.N. and H.H. Kehrler, 1972. Tectonic strain release by underground nuclear explosions and its effect on seismic discrimination, *Geophys. J. R. astr. Soc.*, *31*, 141-161.

- Toksöz, M.N., A. Ben-Menahem, and D.G. Harkrider, 1964. Determination of source parameters of explosions and earthquakes by amplitude equalization of seismic surface waves, *J. Geophys. Res.*, *69*, 4355-4366.
- Wallace, T.C., D.V. Helmberger, and G.R. Engen, 1983. Evidence of tectonic release from underground nuclear explosions in long-period P waves, *Bull. Seism. Soc. Am.*, *73*, 593-613.
- Wallace, T.C., D.V. Helmberger, and G.R. Engen, 1985. Evidence of tectonic release from underground nuclear explosions in long-period S waves, *Bull. Seism. Soc. Am.*, *75*, 157-174.
- Winterstein, D.F., 1986. Anisotropy effects in P-wave and SH-wave stacking velocities contain information on lithology, *Geophysics*, *51*, 661-672.
- Virieux, J., 1986. P-SV wave propagation in heterogeneous media: Velocity-stress finite-difference method, *Geophysics*, *51*, 889-901.

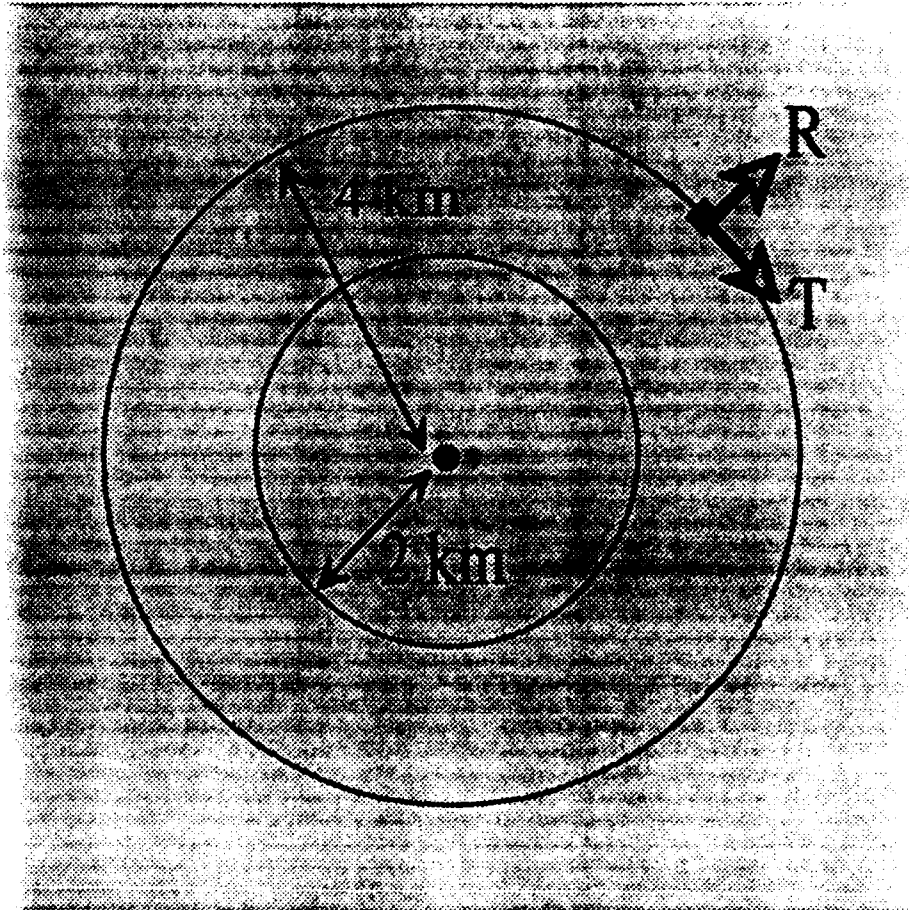
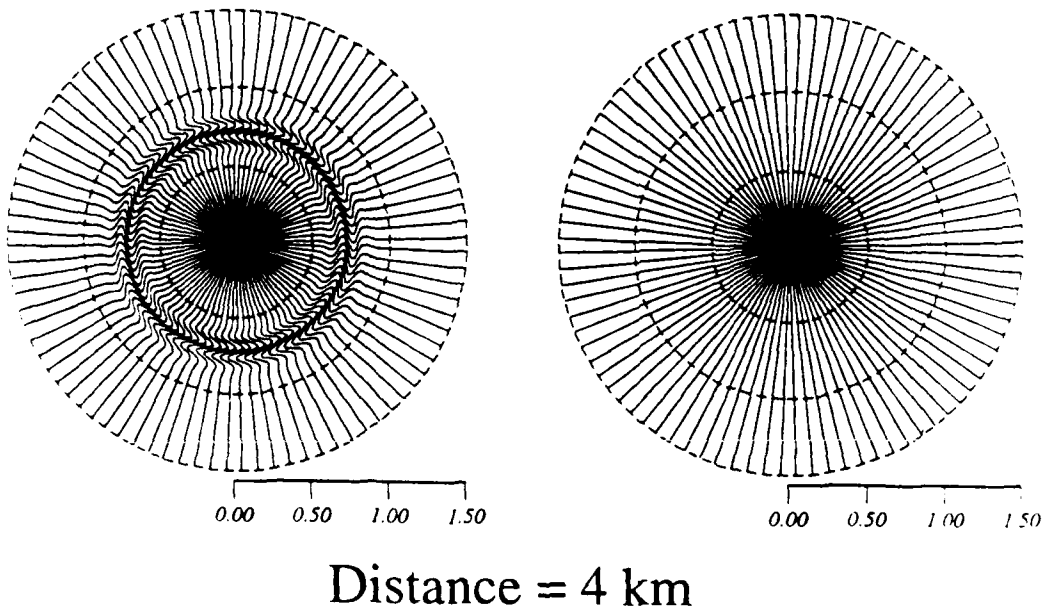
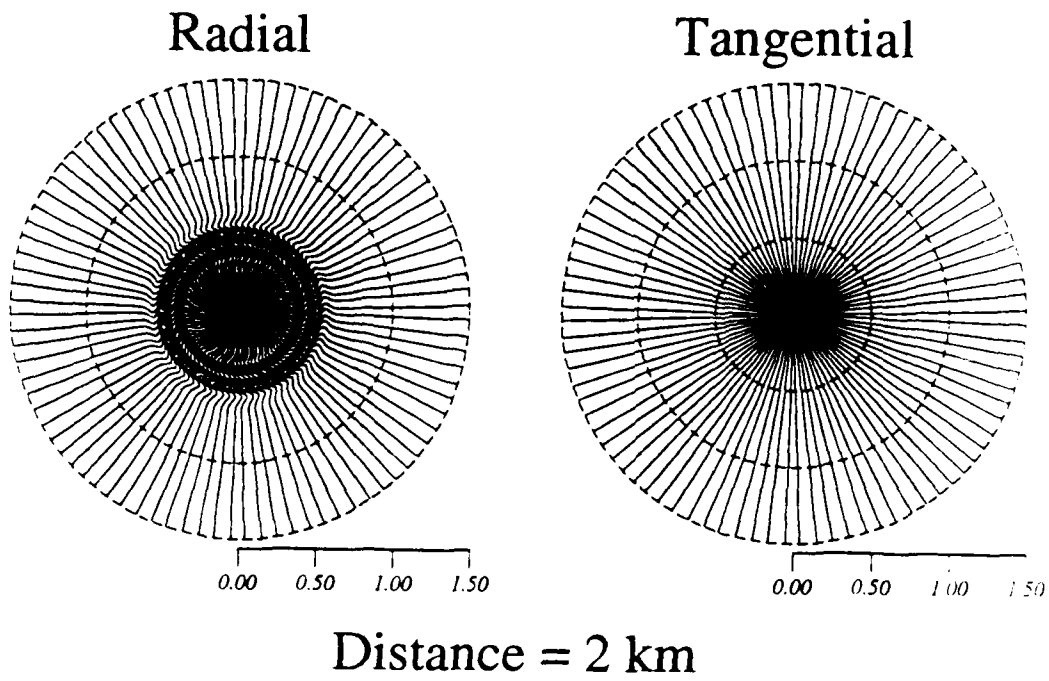
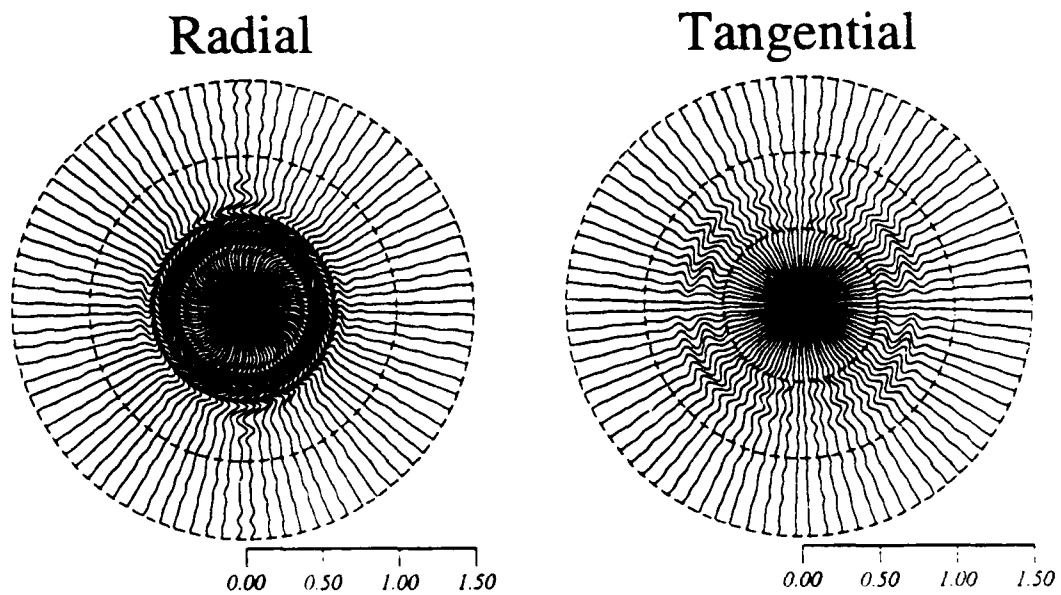


Figure 1: Schematic diagram of the source and receiver geometry used in the synthetic seismogram calculations. There are two vertical circular receiver arrays at radii 2 km and 4 km, respectively, from the source. The *radial* (the particle velocity along the direction of the radial line) and *transverse* (perpendicular to the radial line) motions are illustrated.

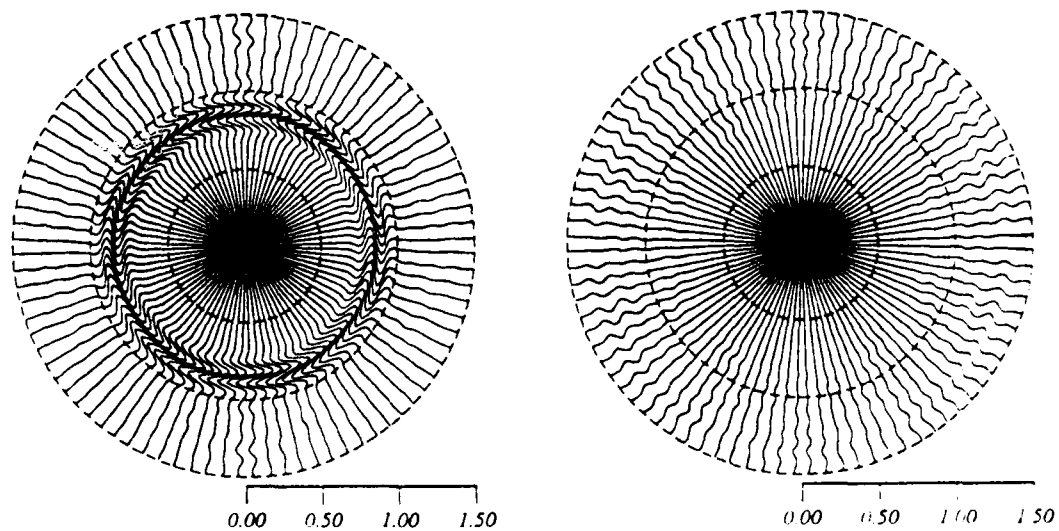


Isotropic Medium, $V_p=6$ Km/S, $V_s=3.46$ Km/S, $f_c = 5$ Hz

Figure 2: Radiation patterns of an explosive source in a homogeneous, isotropic background medium. The radiation pattern is displayed as waveforms computed at circular arrays at a radius of 2 km (top) and 4 km (bottom).



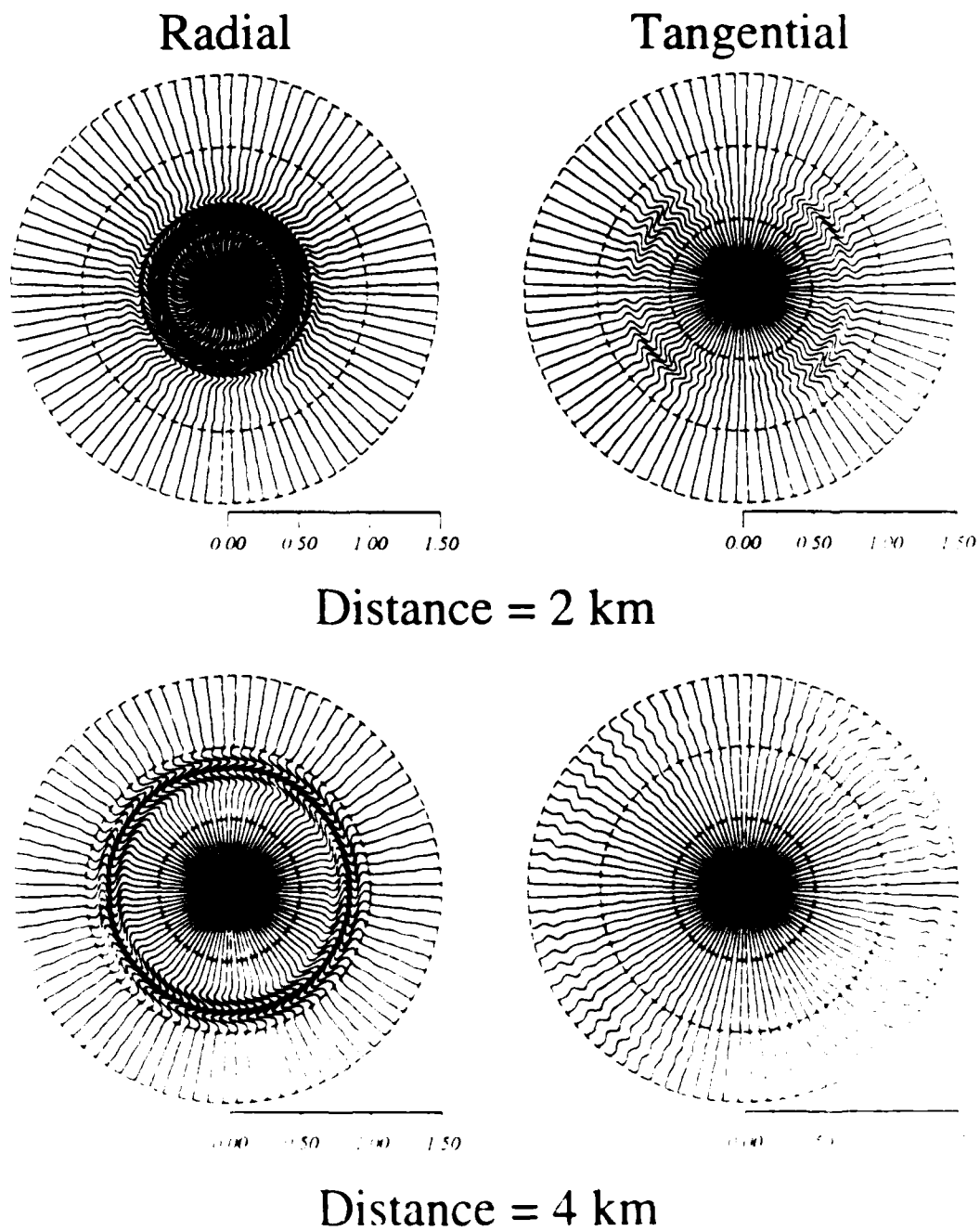
Distance = 2 km



Distance = 4 km

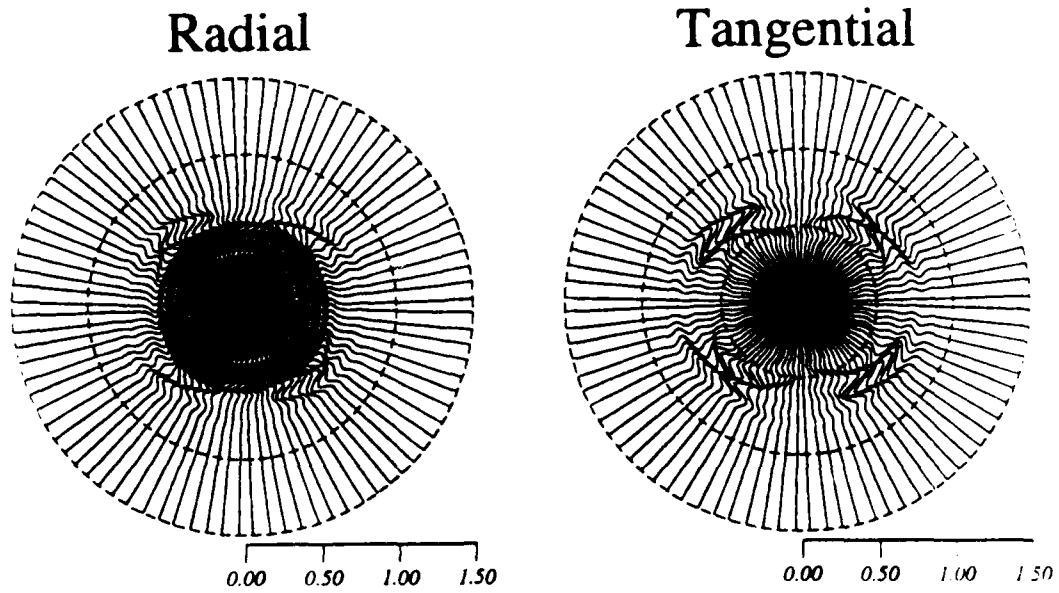
Heterogeneous-01, $f_c = 5$ Hz

Figure 3: Radiation patterns in a randomly heterogeneous medium (Hetero-1) having a 5% r.m.s. variation in parameters and an exponential correlation function with vertical and horizontal correlation lengths of 0.5 km.

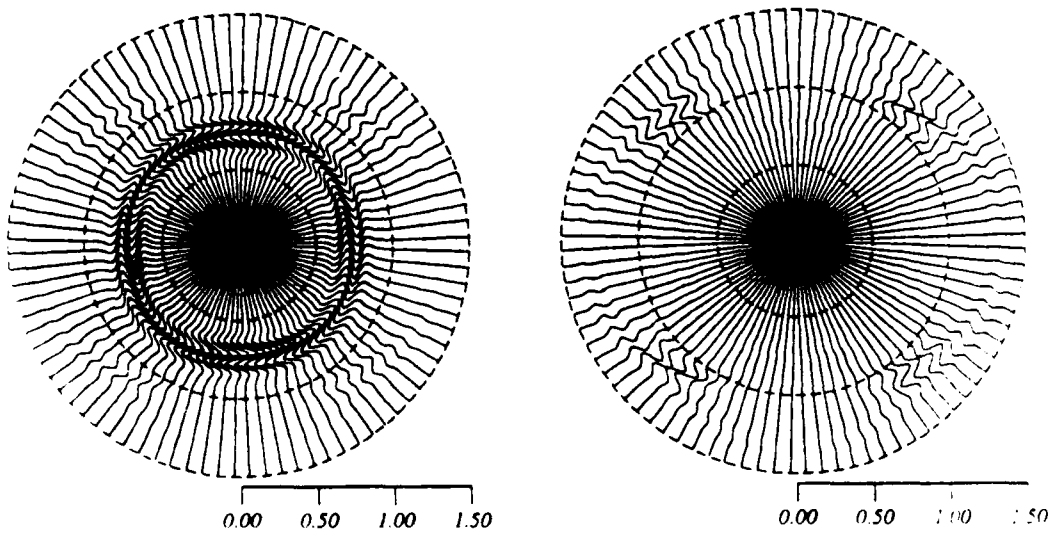


Heterogeneous-020, $f_c = 5$ Hz

Figure 4: Radiation patterns in a randomly heterogeneous medium (Hetero-2) with a vertical correlation length of 0.5 km and horizontal correlation length of 5.0 km. The medium has an exponential correlation function and 5% r.m.s. variation, as in Figure 3.



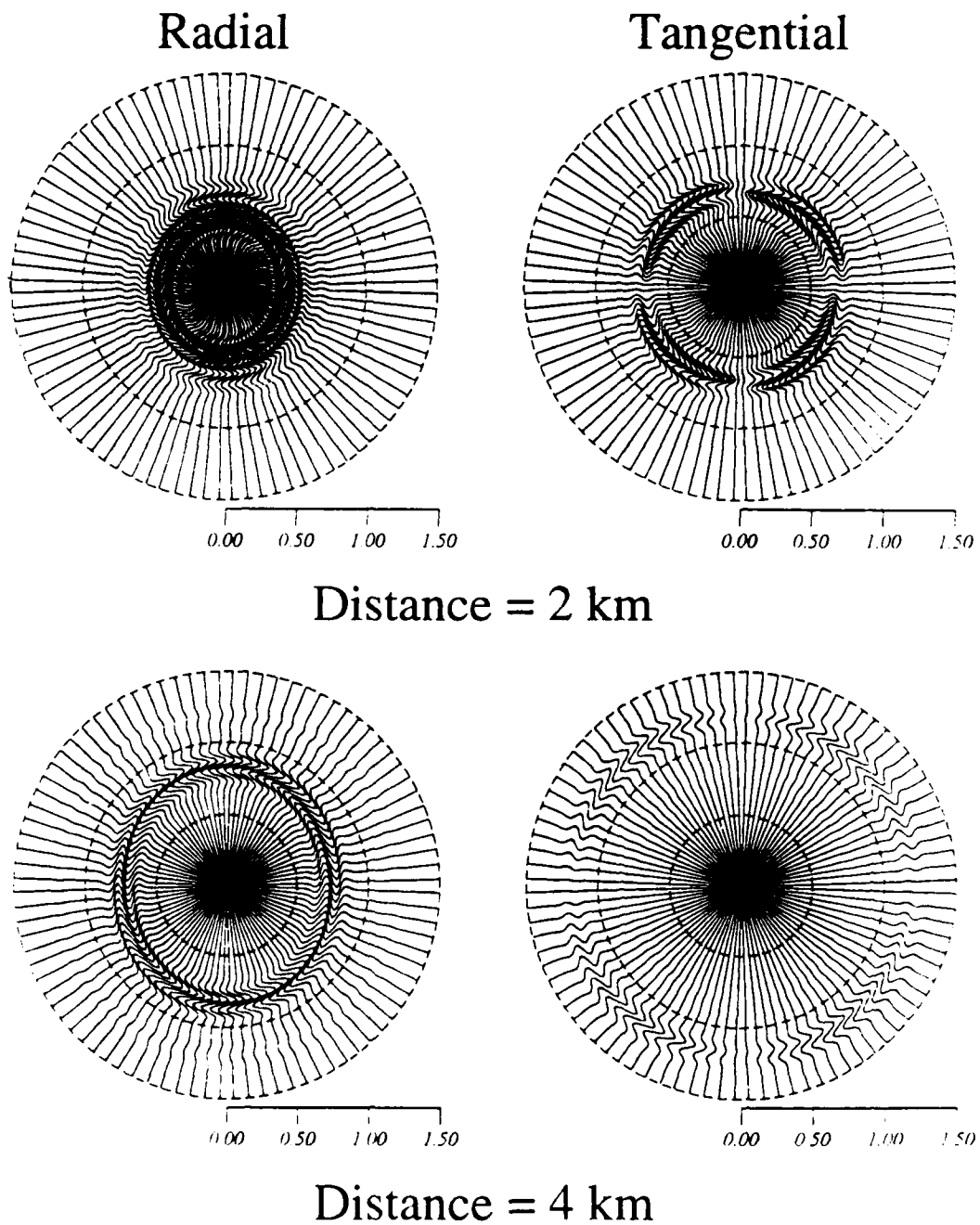
Distance = 2 km



Distance = 4 km

Anisotropic Medium (Micro Fracture), $f_c = 5$ Hz

Figure 5: Radiation patterns in a micro-fractured, anisotropic medium (Micro). The medium is simulated by aligned penny-shaped micro-fractures in the reference isotropic medium. The five elastic constants are evaluated for the equivalent medium with 10% fracture density and 0.001 aspect ratio.



Anisotropic Medium (Joints), $f_c = 5$ Hz

Figure 6: Radiation patterns in a macro-fractured anisotropic medium (Joints). The medium is simulated by aligned joints or macro-fractures in the reference isotropic medium. The medium contains 100 joints/meter with specific stiffness 15×10^{12} Pa/m.

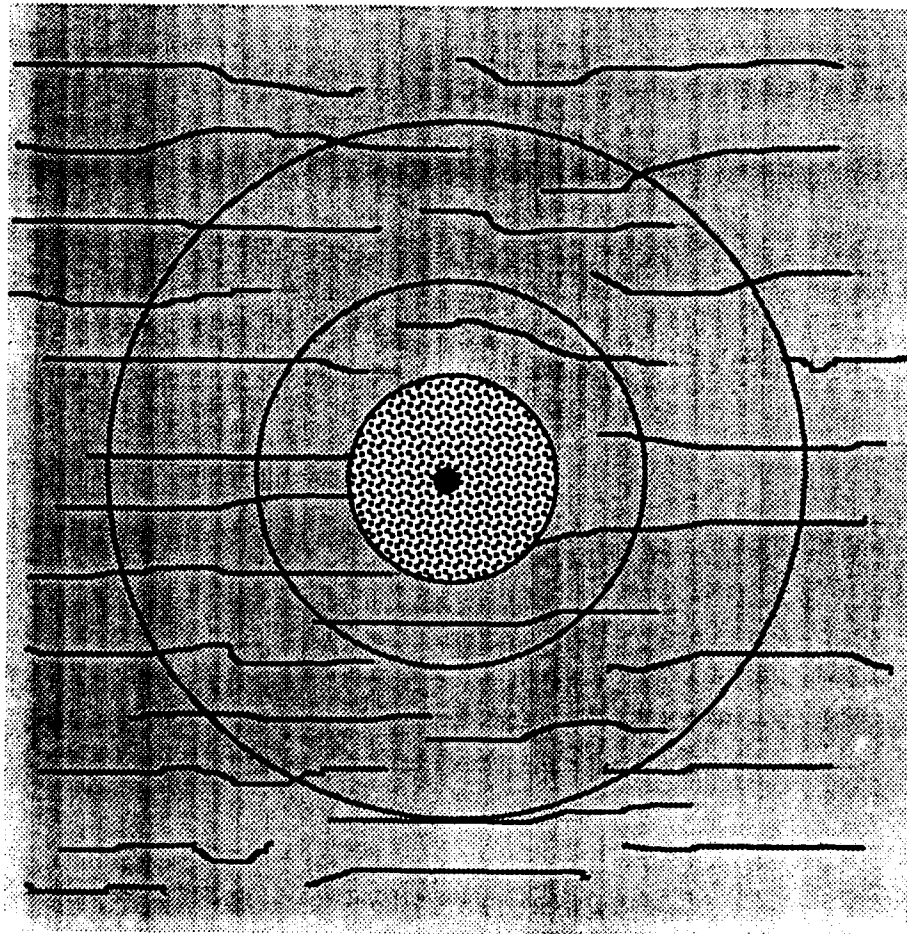
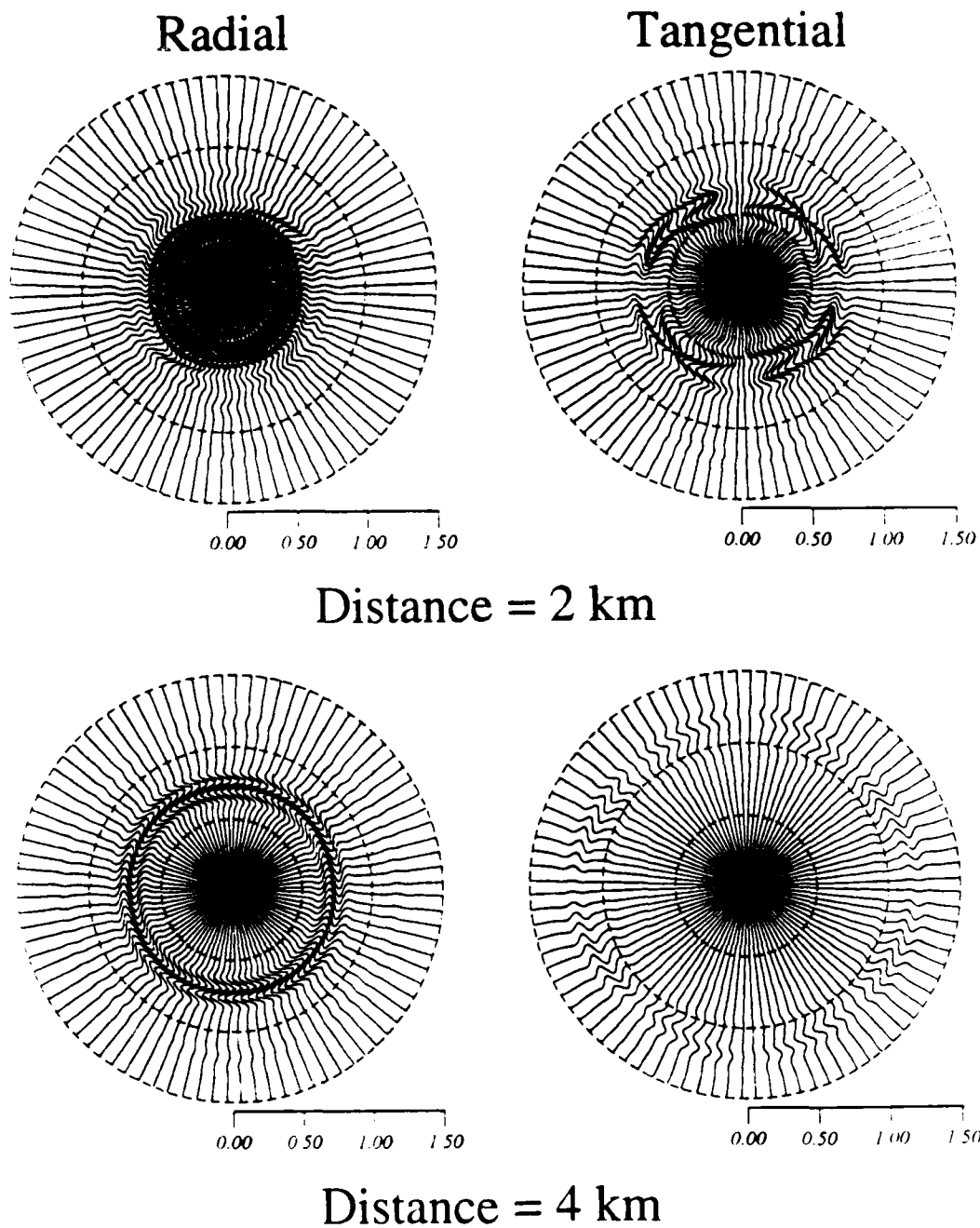
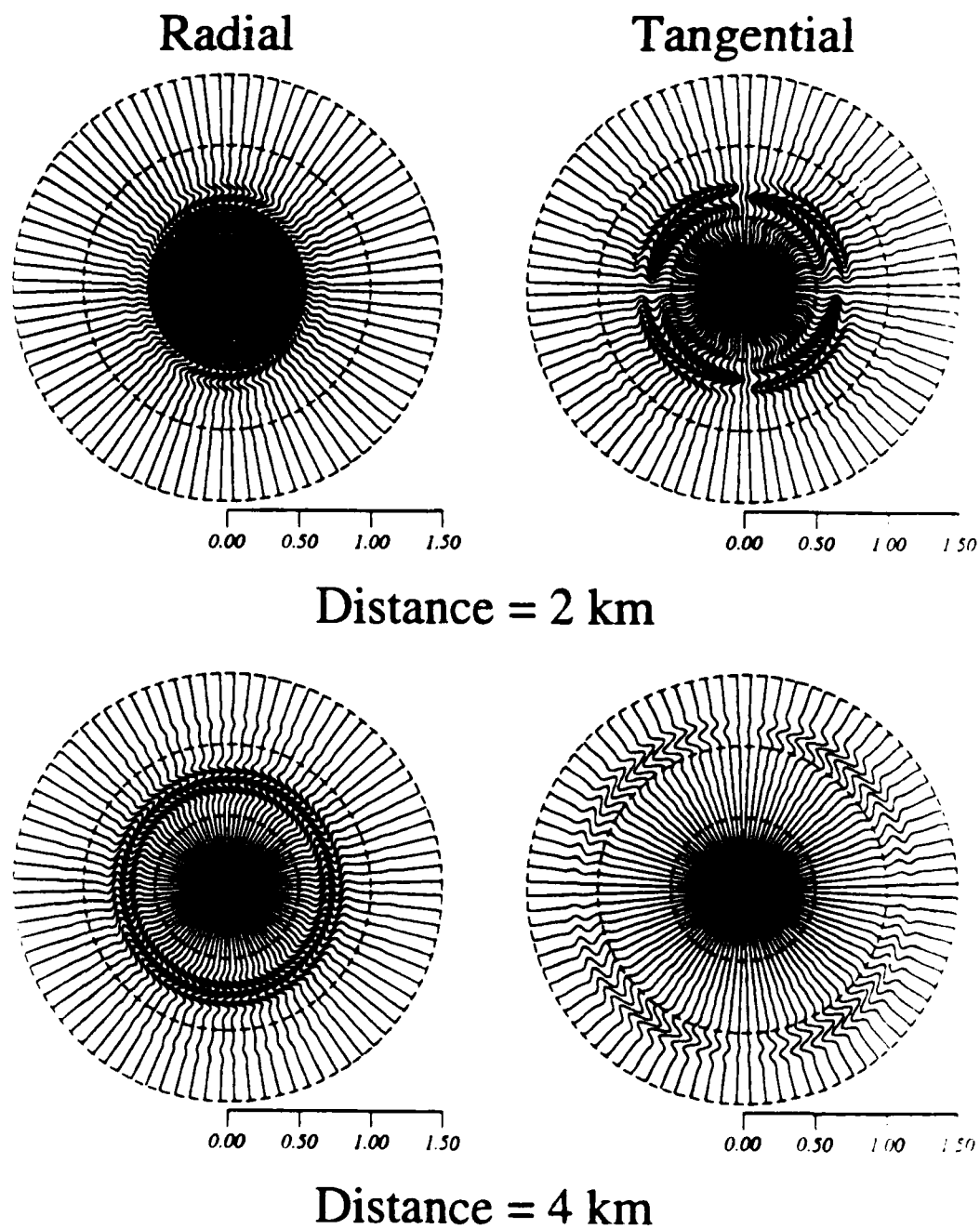


Figure 7: Schematic diagram of a composite model in which the source and propagation media are different.



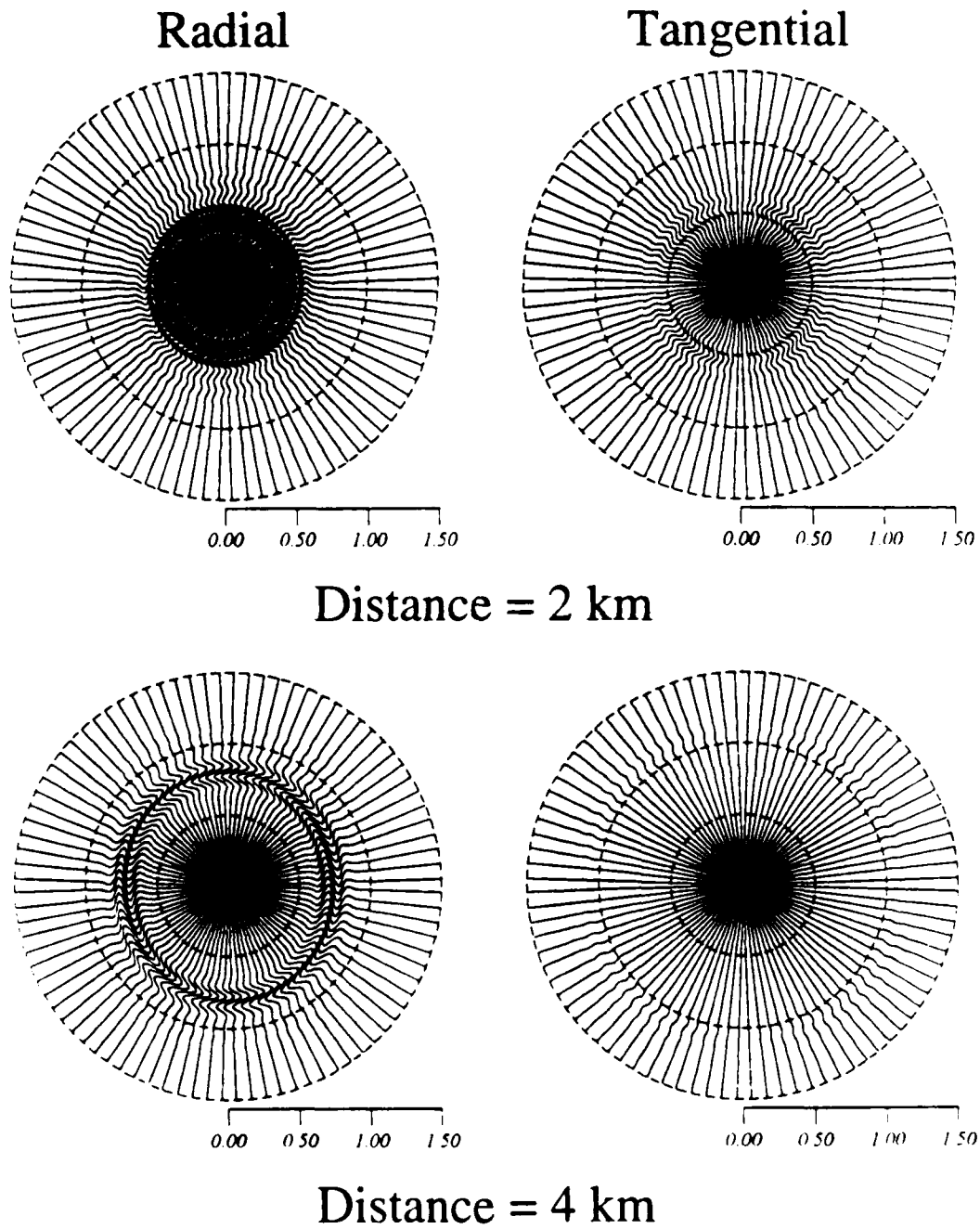
1 km Micro Fracture + Isotropic Medium. $f_c = 5$ Hz

Figure 8: Radiation patterns in a composite model (Micro_Iso). The source medium (inside 1 km radius) is the micro-fracture, anisotropic medium (Micro, used in Figure 5) and the propagation medium is the isotropic, homogeneous background (used in Figure 2).



1 km Joints + Isotropic Medium, $f_c = 5$ Hz

Figure 9: Radiation patterns in a composite model (Joints_Iso). The source medium is the macro-fracture, anisotropic medium (Joints, used in Figure 6) and the propagation medium is the isotropic, homogeneous background.

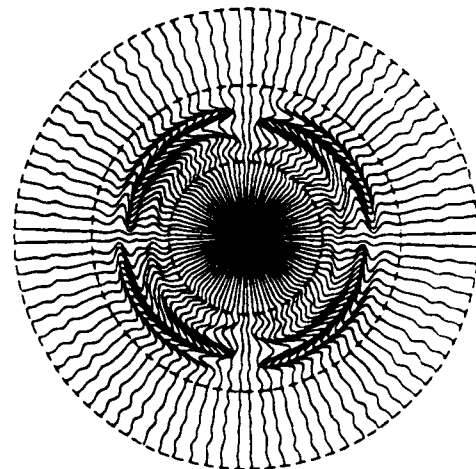
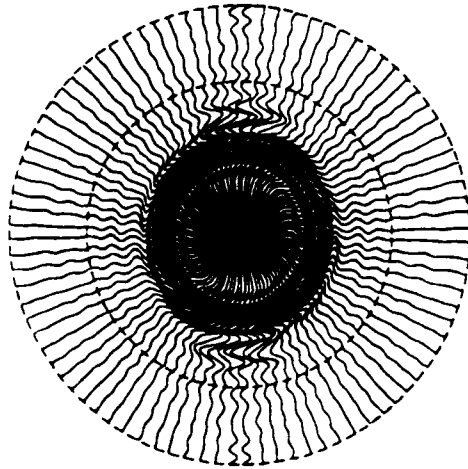


1 km Isotropic Medium + Joints, $f_c = 5$ Hz

Figure 10: Radiation patterns in a composite model (Iso_Joints). The source medium is the background medium and the propagation medium is the macro-fracture, anisotropic medium (Joints, Figure 6).

Radial

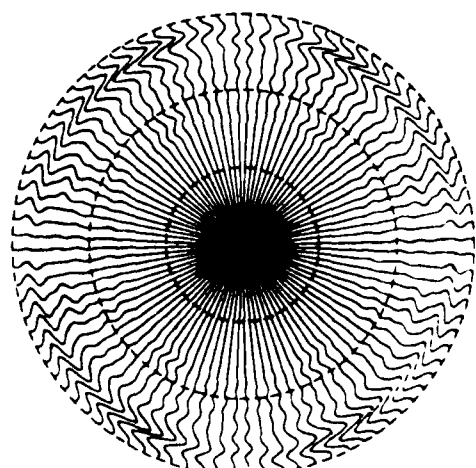
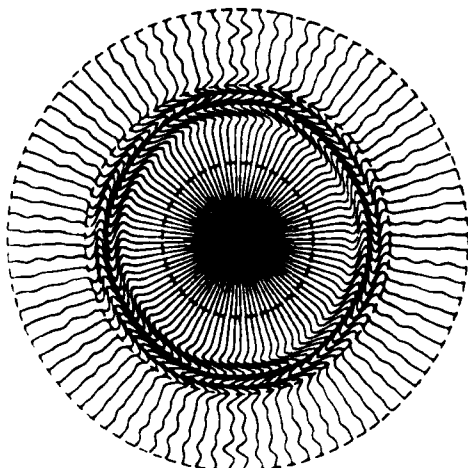
Tangential



0.00 0.50 1.00 1.50

0.00 0.50 1.00 1.50

Distance = 2 km



0.00 0.50 1.00 1.50

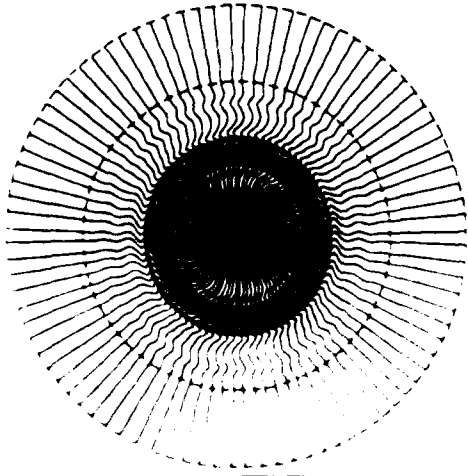
0.00 0.50 1.00 1.50

Distance = 4 km

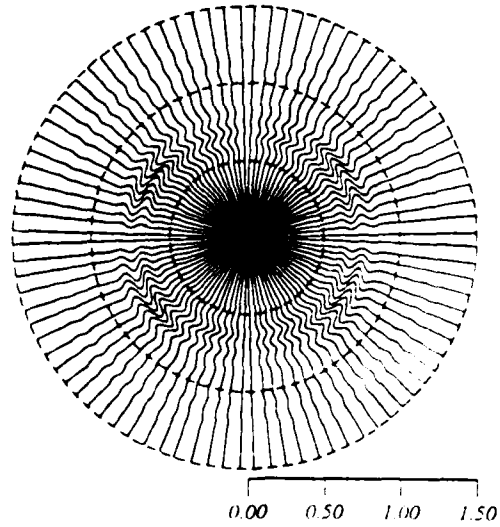
Macro + Hetero-01, $f_c = 5$ Hz

Figure 11: Radiation patterns in a composite model (Joints_Hetero-1). The source medium is the macro-fracture, anisotropic medium (Joints, Figure 6) and the propagation medium is the randomly heterogeneous medium (Hetero-1, Figure 3).

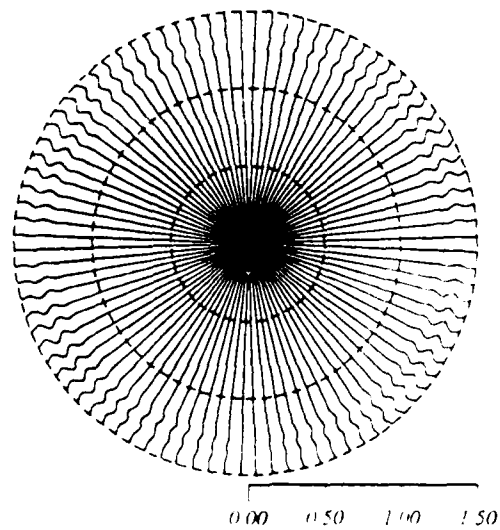
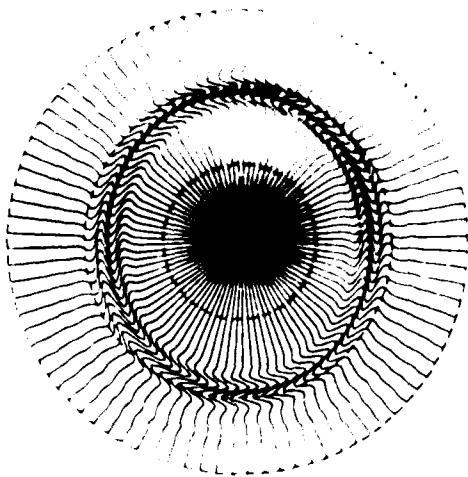
Radial



Tangential



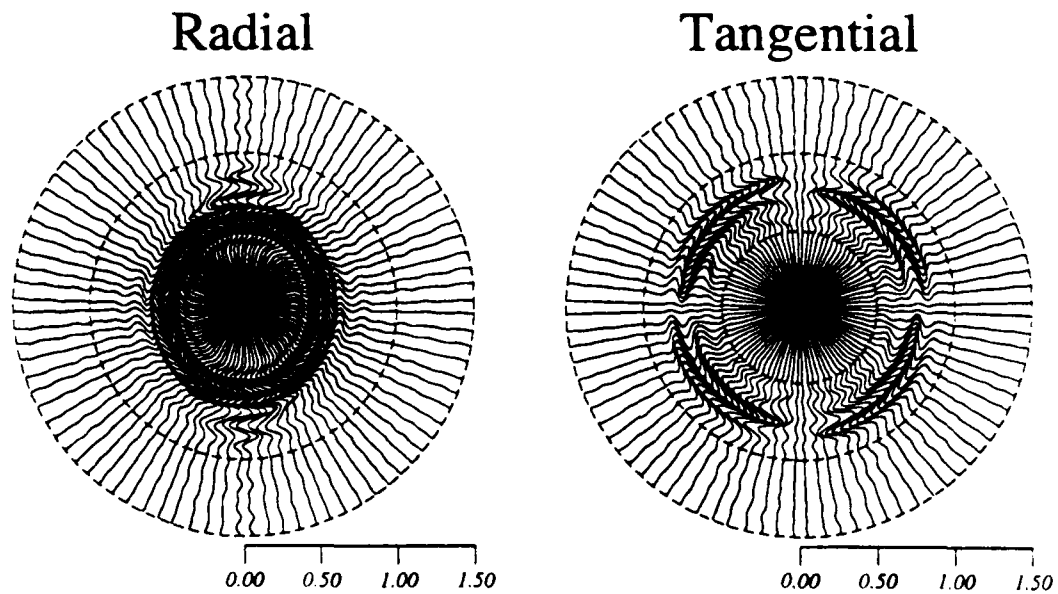
Distance = 2 km



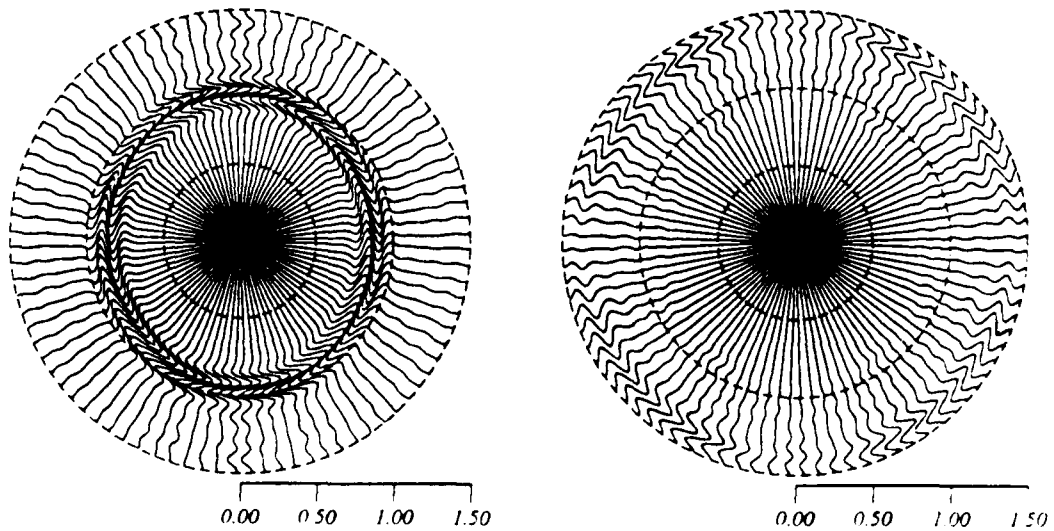
Distance = 4 km

Hetero_01 + Macro. t_c = 5 Hz

Figure 12: Radiation patterns in a composite model (Hetero-1_Joints). The source medium is the heterogeneous model (Hetero-1, Figure 3) and the propagation medium is the macro fracture, anisotropic medium (Joints, Figure 6).



Distance = 2 km



Distance = 4 km

Aniso_hetero-01, $f_c = 5$ Hz

Figure 13: Radiation patterns in a medium which is both randomly heterogeneous and anisotropic (Hetero+Joints). This medium is created by randomly varying all of the anisotropic elastic constants. The anisotropic model is a joint model consisting of 50 joints/meter with specific stiffness 15×10^{12} Pa/m. The heterogeneous fluctuations have a 5% r.m.s. variation and an exponential correlation function with vertical and horizontal correlation lengths of 0.5 km.

2 Km

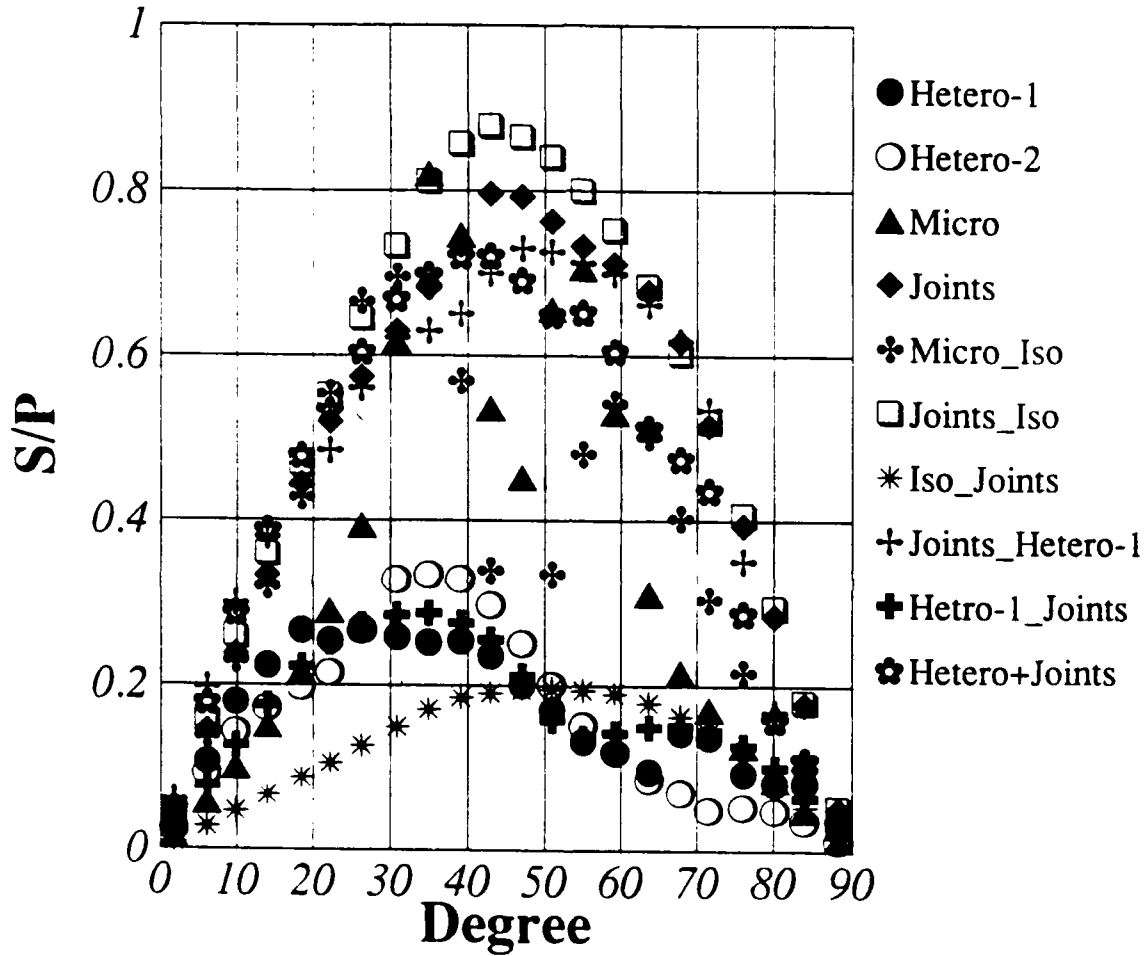


Figure 14: The S wave to P wave amplitude ratio at the 2 km circular array. The P/S ratios are shown for the ten different models used in Figures 3-6 and 8-12. The x-axis is the propagation direction (take-off angle) from the source, varying from horizontal (0°) to vertical (90°). In anisotropic media, the horizontal direction is parallel to the fractures while the vertical direction is perpendicular to the fractures.

4 Km

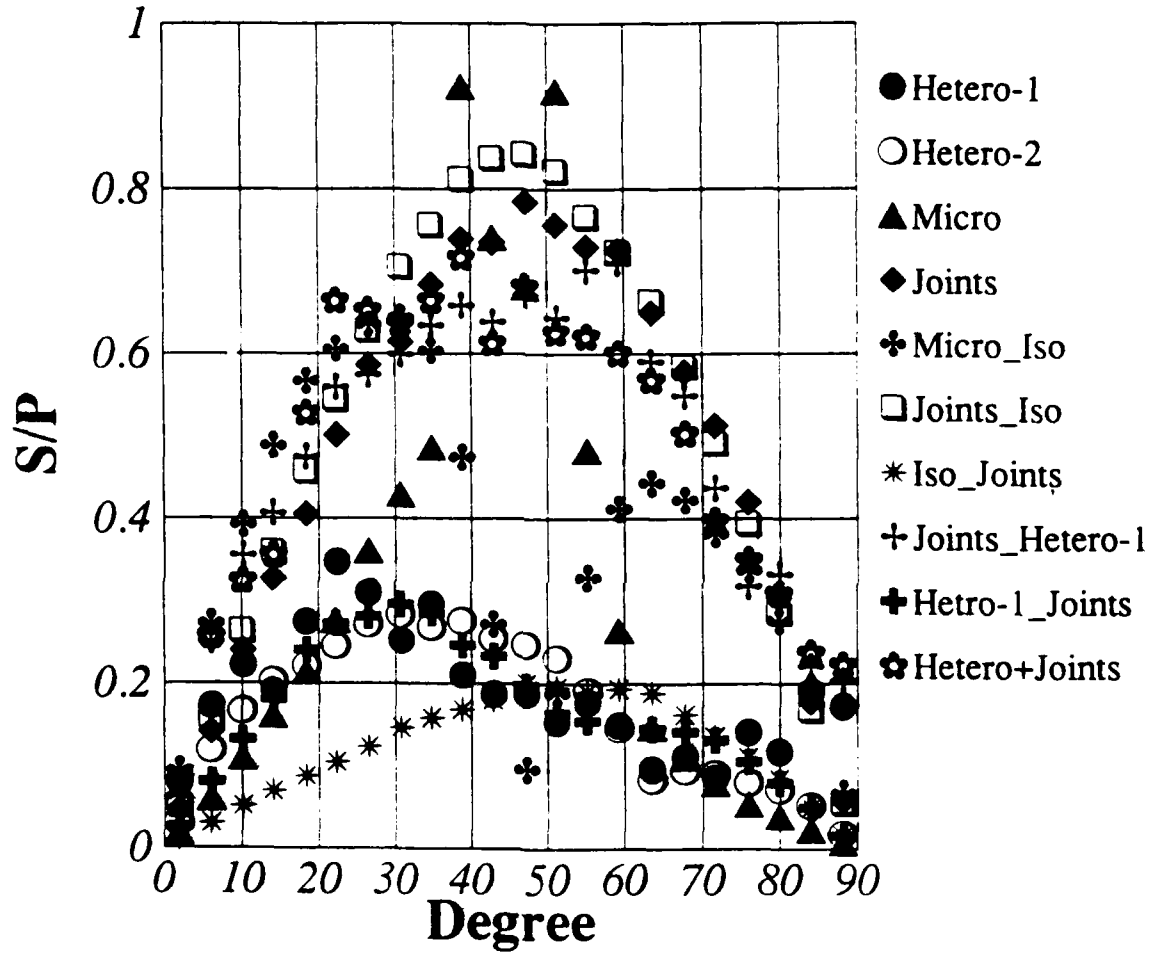


Figure 15: The S/P amplitude ratio at the 4 km circular array, shown in the same format as Figure 14.

SCALE OF ANISOTROPY: A THEORETICAL STUDY OF VELOCITY ANISOTROPY FOR MICRO- AND MACRO-FRACTURES

Summary

Theoretical calculations are made to compare the anisotropic velocity variations for rock masses having micro- and macro-fractures. We use different hypotheses to compute elastic moduli in these two cases. For micro-fracture models, fracture dimensions are assumed to be very small compared to the wavelength (e.g., Hudson, 1980, 1981). For a rock mass with macro-fractures or joints, the stresses are continuous across the fracture but displacements are discontinuous (e.g., Schoenberg, 1980, 1983; Pyrak-Nolte *et al.*, 1990). Both cases show anisotropic velocity variation but differ in nature. For the micro-fracture model, the crucial parameters are the fracture density ($CD = Na^3/V$) and the aspect ratio ($AR = d/a$), where N is the number of fractures of radius, a , and thickness, d , in volume, V . The macro-fracture model is controlled by the fracture spacing (number of fractures per unit length) and the specific stiffness of the fractures (the ratio of the incremental stress across the fracture to the incremental displacement that the stress produces). The value of the specific stiffness determines the seismic properties of the joints, including the effect of mechanical coupling between the joint surfaces on the transmission properties across the joint. For example, an infinite specific stiffness refers to a welded contact and a zero stiffness represents a free

surface.

In the micro-fracture model, for a fixed crack density the qSH velocity does not depend on the aspect ratio. There are smaller velocity variations for qSV and larger variations for qP with an increase in aspect ratio. Velocity variations for all velocities increase with fracture densities. Velocity variations are also studied for both Hudson's first- and second-order theory. The joint model does not produce azimuthal velocity variations of qSV but gives the (constant) velocity shift for different specific stiffnesses, whereas the velocity variations of qP and qSH waves are similar to the micro-fracture model.

Introduction

The understanding of the seismic anisotropy of various fractured rock masses is important to successfully resolve many geophysical problems, such as understanding the local stress direction, the generation of an SH wave from an explosion source, and the exploitation of fractured hydrocarbon and geothermal reservoirs. Discontinuities ranging in scale from micro-fractures to faults are common within the earth's crust. These discontinuities often occur as nearly parallel groups or sets, and also control the hydraulic and mechanical behavior of rock mass. It is important to locate such discontinuities from seismic information when solving practical geophysical problems. It is often observed that the presence of such discontinuities displays seismic anisotropy in the elastic properties of the rock mass. In this study we discuss two crack systems: (1) a dilute fracture model, or micro-fracture model,

where wavelengths are large compared to the size of the cracks; and (2) a non-welded macro-fracture model where the stresses are continuous but displacements are discontinuous across the fracture. Both cases show seismic velocity anisotropy. Micro-fracture theories have been used in most known investigations. Macro-fracture theories can be applied to systems of parallel joints, faults, etc. that are common in very shallow crust. This is especially relevant to quarry blasts and nuclear explosions. The purpose of this study is to understand and compare the nature of velocity variation with different parameters of the fracture systems derived from existing theories.

Micro-Fracture Model

The use of this type of fracture model to represent crack systems is very common. The theory for computing the effective moduli of a rock mass containing aligned thin fractures or cracks was established by Hudson (1980, 1981). This model assumes that the crack dimension is small compared to the wavelength and that the distribution of parallel penny-shaped cracks is dilute. The effective moduli of the entire rock mass containing such crack systems were established by introducing first- and second-order perturbations to the isotropic elastic moduli of the uncracked rock mass, and incorporating fracture density, aspect ratio, and weakly isotropic filling material. From these effective elastic constants, the seismic velocities of the medium containing parallel cracks were determined.

Hudson Model

Hudson (1980, 1981) established the effective elastic moduli, C_{ijkl} , for a medium with aligned vertical micro-cracks applicable to the propagation of long wavelength seismic waves as:

$$C_{ijkl} = C_{ijkl}^0 + C_{ijkl}^1 + C_{ijkl}^2,$$

where

C_{ijkl}^0 : for uncracked solid,

C_{ijkl}^1 : the first-order perturbation, and

C_{ijkl}^2 : the second-order perturbation of the uncracked solid.

The effective first-order perturbation for the cracks perpendicular to the x -axis (schematic diagram shown in Figure 1) is

C_{ijkl}^1 :

$$C_{1111}^1 = -\frac{cD}{\mu}(\lambda + 2\mu)^2 U_{11}, \quad C_{2222}^1 = C_{3333}^1 = -\frac{cD}{\mu} \lambda^2 U_{11},$$

$$C_{1122}^1 = C_{1133}^1 = -\frac{cD}{\mu} \lambda(\lambda + 2\mu) U_{11}, \quad C_{2233}^1 = -\frac{cD}{\mu} \lambda^2 U_{11},$$

$$C_{2323}^1 = 0 \quad \text{and} \quad C_{1313}^1 = C_{1212}^1 = -\frac{cD}{\mu} \mu^2 U_{33}.$$

Second-order perturbation :

C_{ijkl}^2 :

$$C_{1111}^2 = \frac{\Lambda(CD)^2}{15}(\lambda + 2\mu)^2 U_{11}^2, \quad C_{2222}^2 = C_{3333}^2 = \frac{\Lambda(CD)^2}{15} \frac{\lambda^2}{\lambda + 2\mu} U_{11}^2,$$

$$C_{1122}^2 = C_{1133}^2 = \frac{\Lambda(CD)^2}{15} \lambda U_{11}^2, \quad C_{2233}^2 = \frac{\Lambda(CD)^2}{15} \frac{\lambda^2}{\lambda + 2\mu} U_{11}^2,$$

$$C_{2323}^2 = 0 \quad \text{and} \quad C_{1313}^2 = C_{1212}^2 = \frac{(CD)^2}{15} \Delta U_{33}^2.$$

The U_{11} , U_{33} , Λ and Δ are expressed as:

$$U_{11} = \frac{4}{3} \frac{\lambda + 2\mu}{\lambda + \mu} \frac{1}{1 + K}, \quad U_{33} = \frac{16}{3} \frac{\lambda + 2\mu}{3\lambda + 4\mu} \frac{1}{1 + M},$$

$$\Lambda = 15 \left(\frac{\lambda}{\mu} \right)^2 + 28 \frac{\lambda}{\mu} + 28, \quad \Delta = \frac{2\mu(3\lambda + 8\mu)}{\lambda + 2\mu}$$

where

$$K = \frac{3\kappa' + \frac{4}{3}\mu'}{\pi\mu(AR)} \frac{\lambda + 2\mu}{\lambda + \mu}, \quad M = \frac{4\mu'}{\pi\mu(AR)} \frac{\lambda + 2\mu}{3\lambda + 4\mu}$$

and $\kappa' = \lambda' + 2/3\mu'$ is the bulk modulus of the crack-filling material.

The above derivations are valid when the crack distribution is dilute, i.e., $CD(Na^3/V) \ll 1$. The first-order correction is attributed to a single-scattering effect and the second-order correction represents crack-crack interactions (Hudson, 1980, 1981). The first-order perturbations are linear and the second-order perturbations are nonlinear. The first-order perturbations reduce the elastic moduli from uncracked rock moduli, whereas the second-order corrections add to the effects of crack interactions. To understand more about these corrections we consider a Poisson solid ($\lambda = \mu$) where cracks are filled by fluid

($\mu' = 0$). For this case, the expressions above reduce to:

$$K = \frac{3\kappa'}{2\pi\mu(AR)}, \quad M = 0, \quad \Lambda = 71, \quad \Delta = \frac{22\mu}{3},$$

$$U_{11} = \frac{2}{1+K}, \quad \text{and} \quad U_{33} = \frac{16}{7}.$$

The effective elastic constants are:

$$C_{ijkl} = C_{ijkl}^0 + C_{ijkl}^1 + C_{ijkl}^2:$$

$$C_{1111} = \lambda + 2\mu - 3(CD)(\lambda + 2\mu)\frac{2}{1+K} + \frac{71}{15}(CD)^2(\lambda + 2\mu)^2\frac{4}{(1+K)^2},$$

$$C_{2222} = C_{3333} = \lambda + 2\mu - (CD)\lambda\frac{2}{1+K} + \frac{71}{15}(CD)^2\lambda\frac{4}{3(1+K)^2},$$

$$C_{1122} = C_{1133} = \lambda - (CD)(\lambda + 2\mu)\frac{2}{1+K} + \frac{71}{15}(CD)^2\lambda\frac{4}{(1+K)^2},$$

$$C_{2233} = \lambda - (CD)\lambda\frac{2}{1+K} + \frac{71}{15}(CD)^2\lambda\frac{4}{3(1+K)^2},$$

$$C_{2323} = \mu \quad \text{and} \quad C_{1313} = C_{1212} = \mu - \frac{16}{7}(CD)\mu + \frac{22}{45}(CD)^2\left(\frac{16}{7}\right)^2\mu.$$

Hudson's formulations of the effective elastic moduli may be valid for small crack density as we can see in the expression of the Poisson solid where the effective elastic moduli are negative for large crack density. Examples are shown below.

It is critical to truncate the series of alternate positive and negative elements where one cannot estimate the series correctly unless full series are used. In this case, one should not use this formula for large crack density and aspect ratio. The first-order formula may estimate the elastic moduli correctly when the crack density is near or less than 0.1. The accuracy could be extended by including the second-order formula. Figure 2 shows the

azimuthal variation of normalized velocities with different aspect ratios for a crack density 0.1 for (a) only the first-order case and (b) both the first- and second-order cases, where the parallel cracks in the rock mass are filled with gas and the velocity parameters of the rock mass are 5.0 (V_p) and 2.9 km/sec (V_s). 0° represents the wave propagation perpendicular to the crack plane. As the aspect ratio increases, the velocity variation increases for both qP and qSV waves. The qSH wave variation does not depend on aspect ratios (AR). Note that here we use the terminology qSV and qSH instead of qSP (shear wave parallel to the symmetry axis) and qSR (shear wave right angle to the symmetry axis). Our experience with oil companies and solid earth geophysicists show that it is more convenient to explain the two shear wave velocities as qSH and qSV or by fast ($S1$) and slow ($S2$) shear waves.

Figure 3 represents the velocity variation with different crack densities and aspect ratios for the wave propagating along the plane 60° from the crack plane (i.e., 30° from the perpendicular of the crack plane). In general, the velocity anisotropy increases with an increase in crack density and aspect ratio. However, the velocity anisotropy behaves nonlinearly at higher values of the aspect ratio and crack density. For the first-order case and for large crack densities and aspect ratios, velocities (qP and qSV) go to zero (negative elastic moduli). In such cases, the second-order corrections cause the elastic moduli to become positive. Both the first- and second-order corrections give less velocity anisotropy, as shown in Figures 3a and 3b. The slope of velocity variation changes rapidly at a large fracture density and aspect ratio (Figure 3b). Hudson's model, using both first- and second-order perturbations, is

useful to model a micro-fracture system that may be evenly distributed in the upper crust. One should, however, consider the limitation of the crack density and aspect ratio discussed in this paper.

Macro-Fracture Model

We present the systems of parallel joints, faults, etc. that are common in very shallow crust. This model represents a rock mass containing a single to several non-welded interfaces represented by displacement discontinuity boundary conditions in the seismic wave equation (schematic diagram shown in Figure 4). The displacement discontinuity is the ratio of average stress to the specific stiffness of the interface. The stiffness is related to the density of coplanar fractures. The dense fracture population refers to a low fracture stiffness, while the dilute fracture population represents a high fracture stiffness. The specific stiffness is the ratio of the internal stress across the fracture to the incremental displacement that the stress produces. The value of a specific stiffness determines the seismic properties of the fractures, including the effect of mechanical coupling between the fracture surfaces on the transmission properties across the fracture. For example, an infinite specific stiffness refers to the welded contact and a zero stiffness represents the free surface. In this model the main constraint is that the seismic wavelength must be greater than the fracture spacing (i.e., the asperities of contact between the two surfaces of the fracture). Theoretical studies involving the general solution of the seismic wave equation for this kind of fracture are given

by Schoenberg (1980), Park-Nolte *et al.* (1990), and others. Park-Nolte *et al.* (1990) also investigated the displacement discontinuity theory considering observed laboratory data. This model also produces anisotropic velocity variation that is different in nature from the dilute fracture model.

To compute the velocity variation across the non-welded single fracture separated by two isotropic homogeneous half-spaces (Figure 4), the essential boundary conditions for an incident compressional plane wave impinging on the fracture are:

$$U_x^1 - U_x^2 = \frac{\tau_{xx}}{\kappa_x}, \quad U_y^1 - U_y^2 = \frac{\tau_{xy}}{\kappa_y}, \quad U_z^1 - U_z^2 = \frac{\tau_{zx}}{\kappa_x},$$

$$\tau_{zx}^1 = \tau_{zx}^2 \quad \tau_{zy}^1 = \tau_{zy}^2 \quad \text{and} \quad \tau_{zz}^1 = \tau_{zz}^2,$$

where

U = displacement,

τ = stress,

κ = specific stiffness of the fracture = $\frac{\Delta\tau}{\Delta u}$,

1,2 = superscripts referring sides of the fracture.

Using these boundary conditions to the plane wave, we get a phase shift (Φ_T) of the transmitted wave caused by the non-welded nature of the fracture. For example, the phase shift for a normal incidence wave is given by Park-Nolte *et al.* (1990):

$$\Phi_T = \tan^{-1}\left(\frac{\omega}{2\kappa/Z}\right).$$

The quantity, Z , is seismic impedance, $Z = \rho V$, where ρ is density, and V is the phase

velocity. The angular frequency is denoted by ω . This phase shift is dependent on frequency and the ratio of fracture stiffness to seismic impedance. This phase shift causes a group delay on the transmitted wave, which is given by

$$t_{gT} = \frac{d\Phi}{d\omega}.$$

Since the phase shift depends on fracture stiffness and frequency, the group delay also varies with fracture stiffness and frequency. The effective group time delay, t_{eff} , for a medium containing a set of N parallel fractures can be obtained from

$$t_{eff} = \frac{L}{V_G \cos\theta} + Nt_{gT},$$

where

V_G : group velocity of the unfractured rock,

L : total path length along the line normal to the fracture planes,

θ : angle of incidence (0° : perpendicular to the fracture planes).

Now we can compute effective group velocity from the relation

$$V_{Geff} = \frac{L/\cos\theta}{t_{eff}}.$$

This effective group velocity depends on the angle of incidence, the ratio of the specific stiffness of the fracture to the seismic impedance of the unfractured rock, and the frequency of

the plane wave. Figure 5 shows the normalized group velocity variations with an incidence angle of different frequencies. These theoretical results show that the variation of velocities are constant for a lower frequency band (0-5,000 Hz). A certain irregularity in the qSV wave (near 32° incidence) is due to the critical angle for a converted P wave generated by an incident SV wave. The velocity jump at 90° evaluates the same velocity of the unfractured rock velocity as the above relation. We also compute the velocity variation (independent of frequency) using Schoenberg's (1983) average strain method. The effective moduli for the x -axis perpendicular to the fracture planes are given by

C_{ijkl} :

$$C_{1111} = \frac{\mu}{\gamma + E_N}, \quad C_{2222} = C_{3333} = [1 + 4(1 - \gamma)E_N]C_{1111},$$

$$C_{1122} = C_{1133} = (1 - 2\gamma)C_{1111},$$

$$C_{2323} = \mu, \quad C_{1313} = C_{1212} = \frac{\mu}{1 + E_T},$$

where

$$E_N = \frac{\mu N}{\kappa_N}, \quad E_T = \frac{\mu N}{\kappa_T} \quad \text{and} \quad \gamma = \frac{1 - 2\sigma}{2(1 - \sigma)} = \frac{\beta^2}{\alpha^2}.$$

The normal and transverse specific stiffnesses are κ_N and κ_T , respectively. As usual the P and S velocities of the intact rock mass are α and β , respectively. The azimuthal velocity variations from the moduli using the average strain method are shown in Figure 6. Figure 7 shows a similar velocity variation (for higher specific stiffnesses) using a non-welded fracture model with the displacement discontinuity boundary condition to the plane wave. From Fig-

ures 6 and 7 we conclude that the average strain method produces similar velocity variations at low frequencies for the non-welded fracture model, except the 90° velocity jump (Figures 5 and 7). Several interesting features are observed: (1) the velocity variations for qP and qSH waves are similar to the microfracture model; (2) qSV waves are entirely different; and (3) there is no azimuthal velocity variation for qSV waves but there is a constant shift for different specific stiffnesses for the non-welded fracture model. Figure 8 shows the velocity variation with the number of fractures per unit length and with different specific stiffnesses for the wave propagating along the plane 60° from the fracture plane.

Comparing the two models, Figure 9 illustrates their differences. In some cases we can compare the specific stiffness, the aspect ratio, and the fracture per unit length with crack density for the macro- and micro-fracture models. In this comparison, we consider the different parameters so that the differences of qP velocity variations are minimized. Both models are important in interpreting seismic data and in resolving important questions concerning the physical processes in subsurface structures.

Discussion

We review anisotropic velocity variations due to aligned fractures distributed evenly in the rock mass. The two theoretical approaches contribute different velocity variations. In some cases, the results from these two methods could be correlated. Our study needs further experimental data to confirm the theoretical predictions. In general, the difference between

the two approaches could result in significantly different interpretations of the field data.

References

- Hudson, J.A., 1980. Overall properties of a cracked solid, *Math. Proc. Cambridge Philos. Soc.*, 88, 371-384.
- Hudson, J.A., 1981. Wave speeds and attenuation of elastic waves in material containing cracks, *Geophys. J. R. astr. Soc.*, 64, 133-150.
- Pyrak-Nolte, L.J., L.R. Myer, and N.G.W. Cook, 1990, Anisotropy in seismic velocities and amplitudes from multiple parallel fractures, *J. Geophys. Res.*, 95, 11345-11358.
- Schoenberg, M., 1980. Elastic wave behavior across linear slip interfaces, *J. Acoust. Soc. Am.*, 68, 1516-1521.
- Schoenberg, M., 1983. Reflection of elastic waves from periodically stratified media with interfacial slip, *Geophys. Prospect.*, 31, 265-292.

Micro-fracture Model

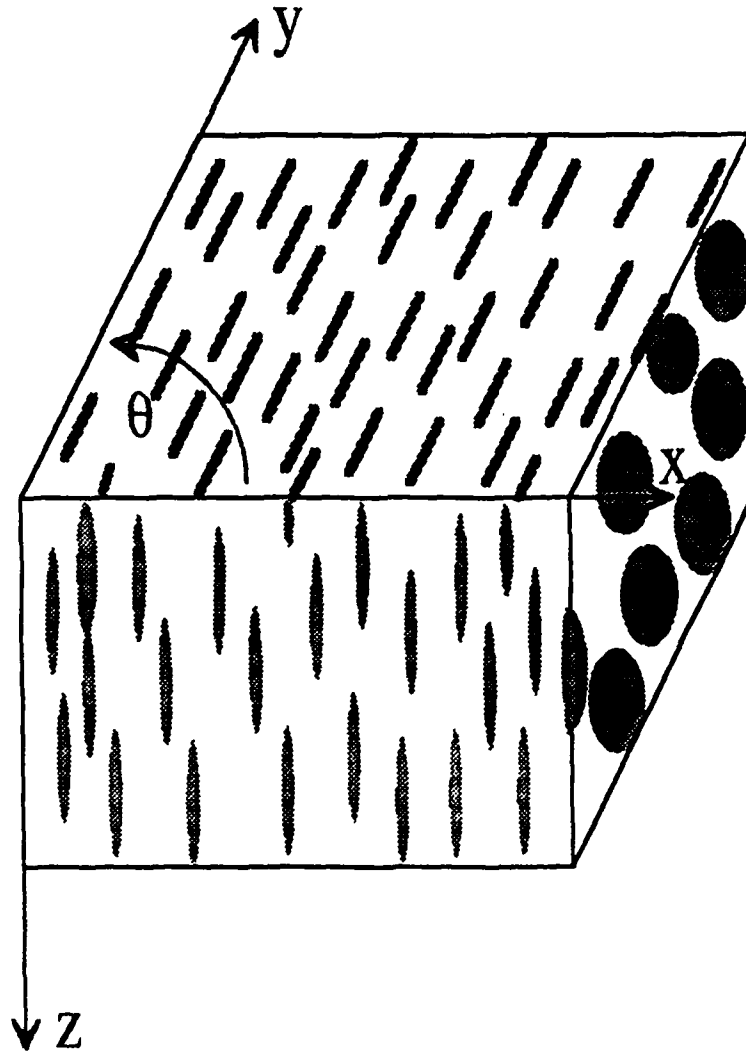


Figure 1: Schematic diagram of the micro-fracture model. The x -axis is the symmetry axis and perpendicular to the fracture plane.

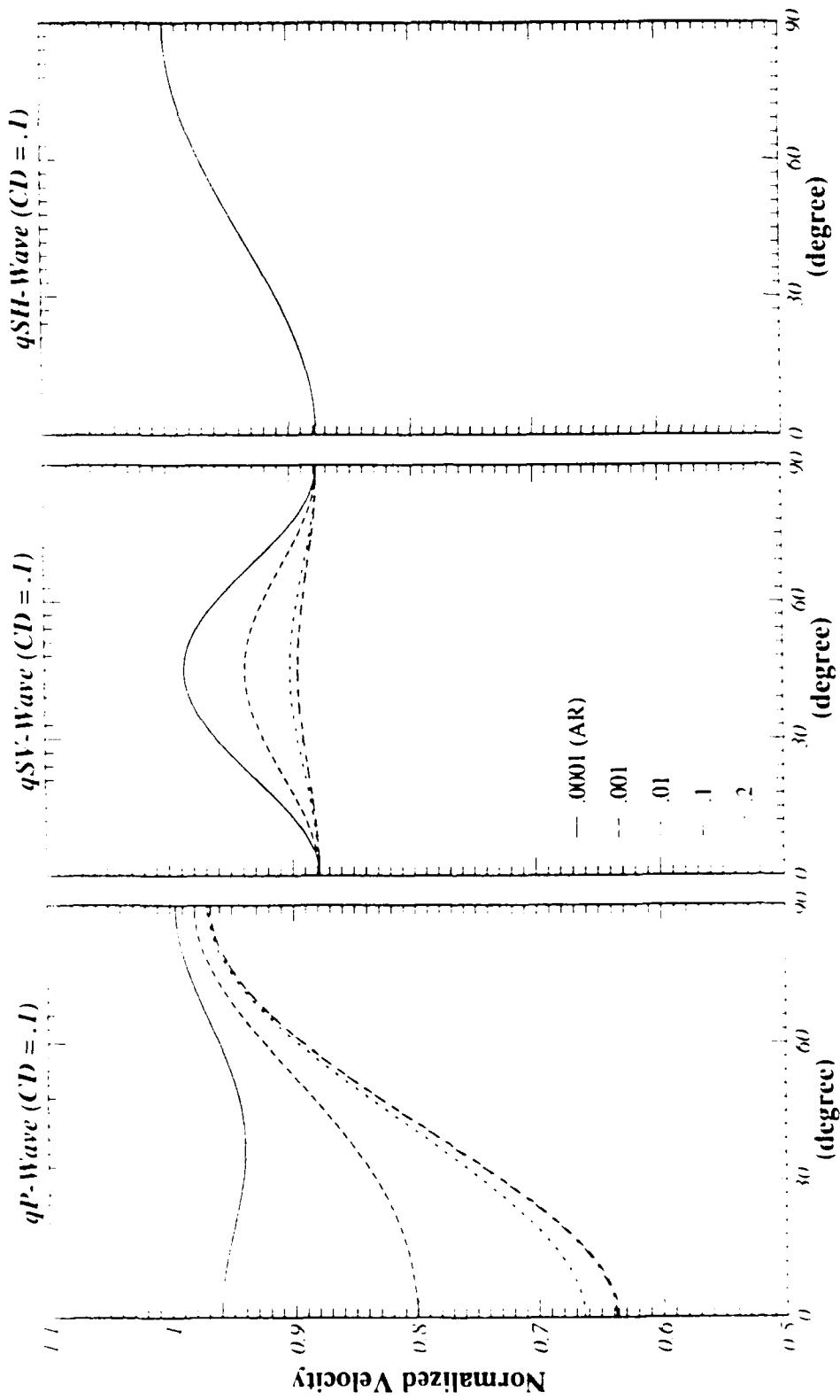


Figure 2a: Normalized azimuthal velocity as a function of the aspect ratio for a crack density of 0.1 using the first-order Hudson theory. 0° represents the wave incident perpendicular to the fractures. The unfractured rock velocities are 5.0 (Vp) and 2.9 km/sec (Vs).

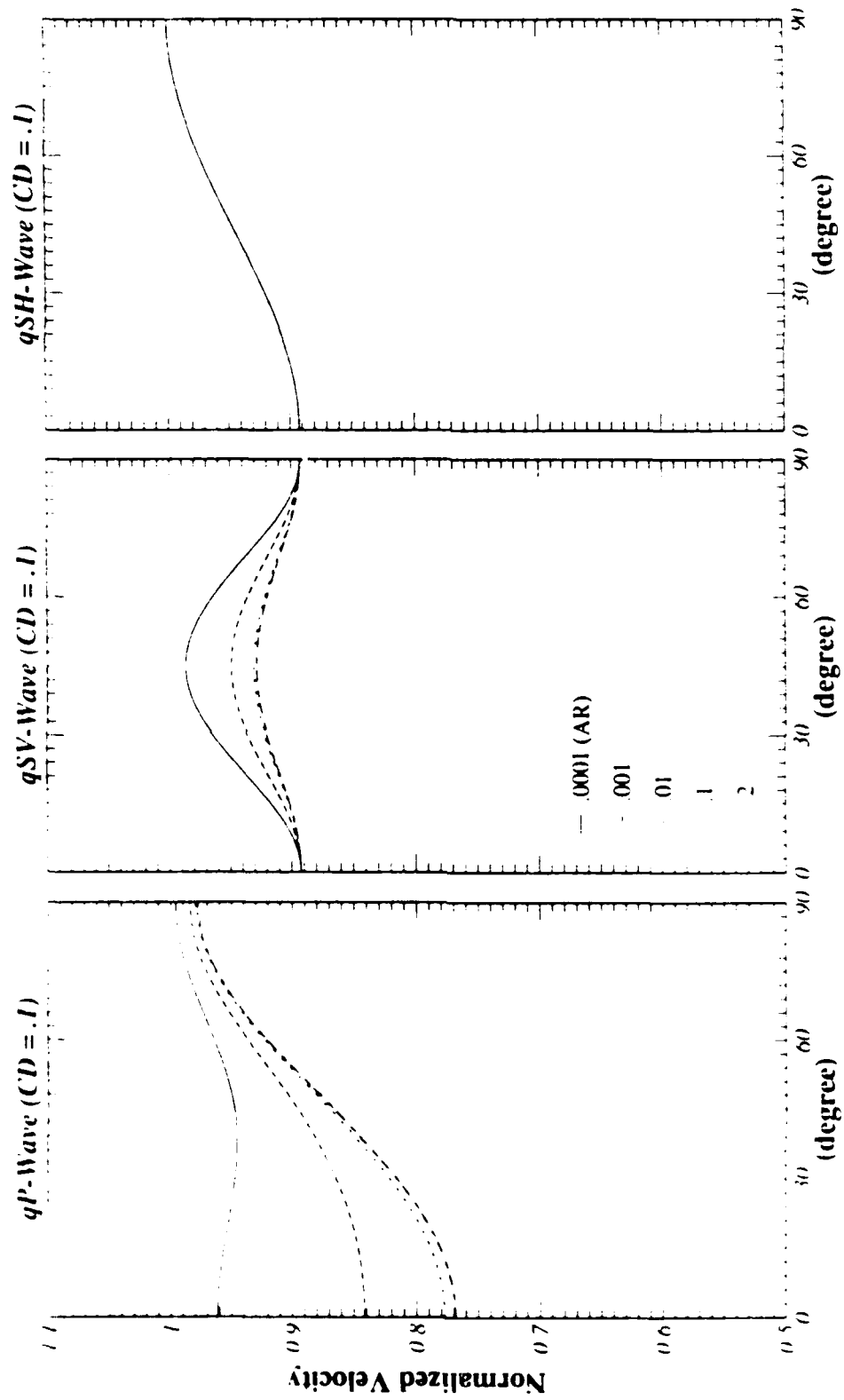


Figure 2b: Normalized azimuthal velocity as a function of the aspect ratio for a crack density of 0.1, including the second-order Hudson theory. 0° represents the wave incident perpendicular to the fractures.

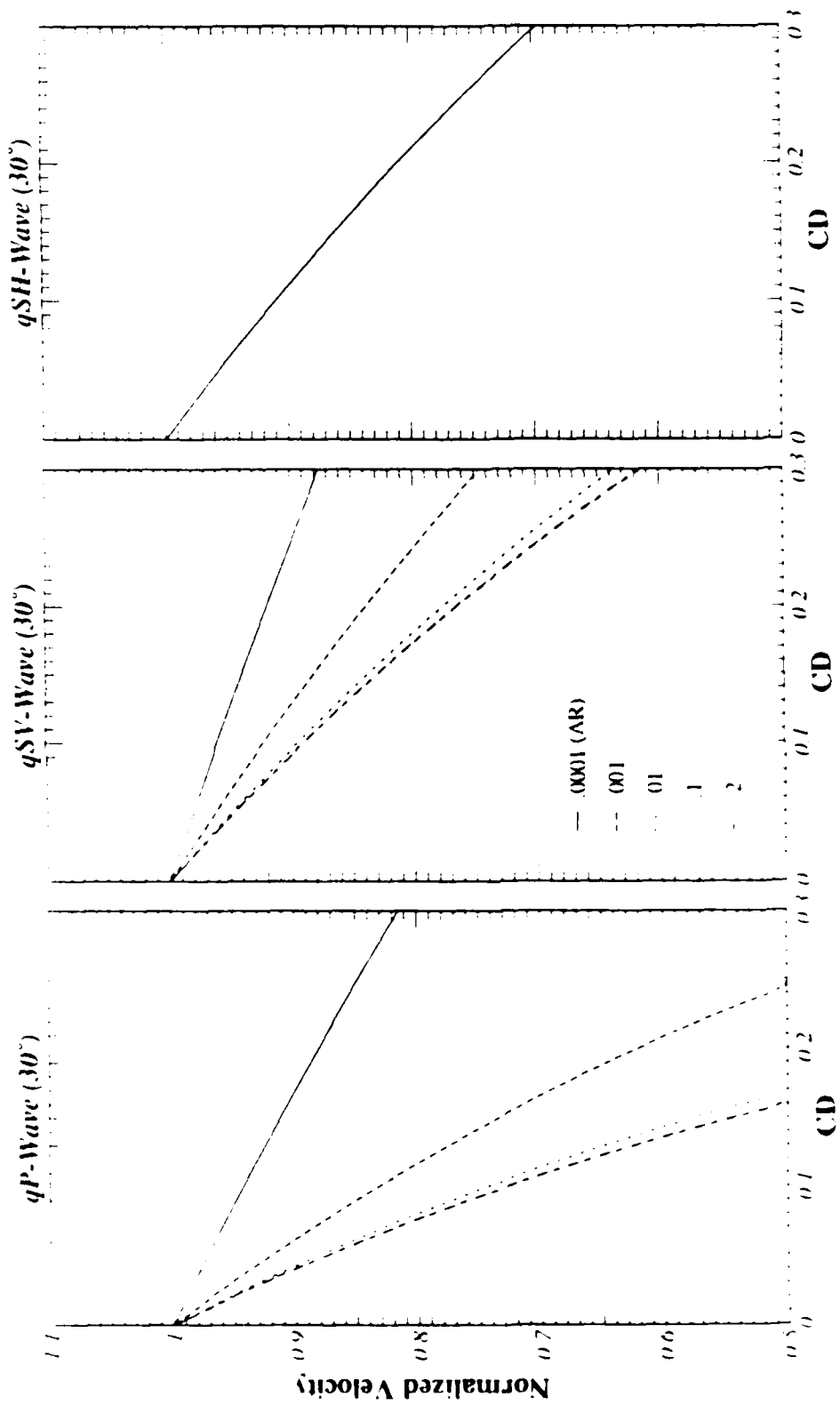


Figure 3a Normalized velocity as a function of crack density and the aspect ratio for the wave incidence at 30° perpendicular to the crack plane using only the first-order Hudson theory.

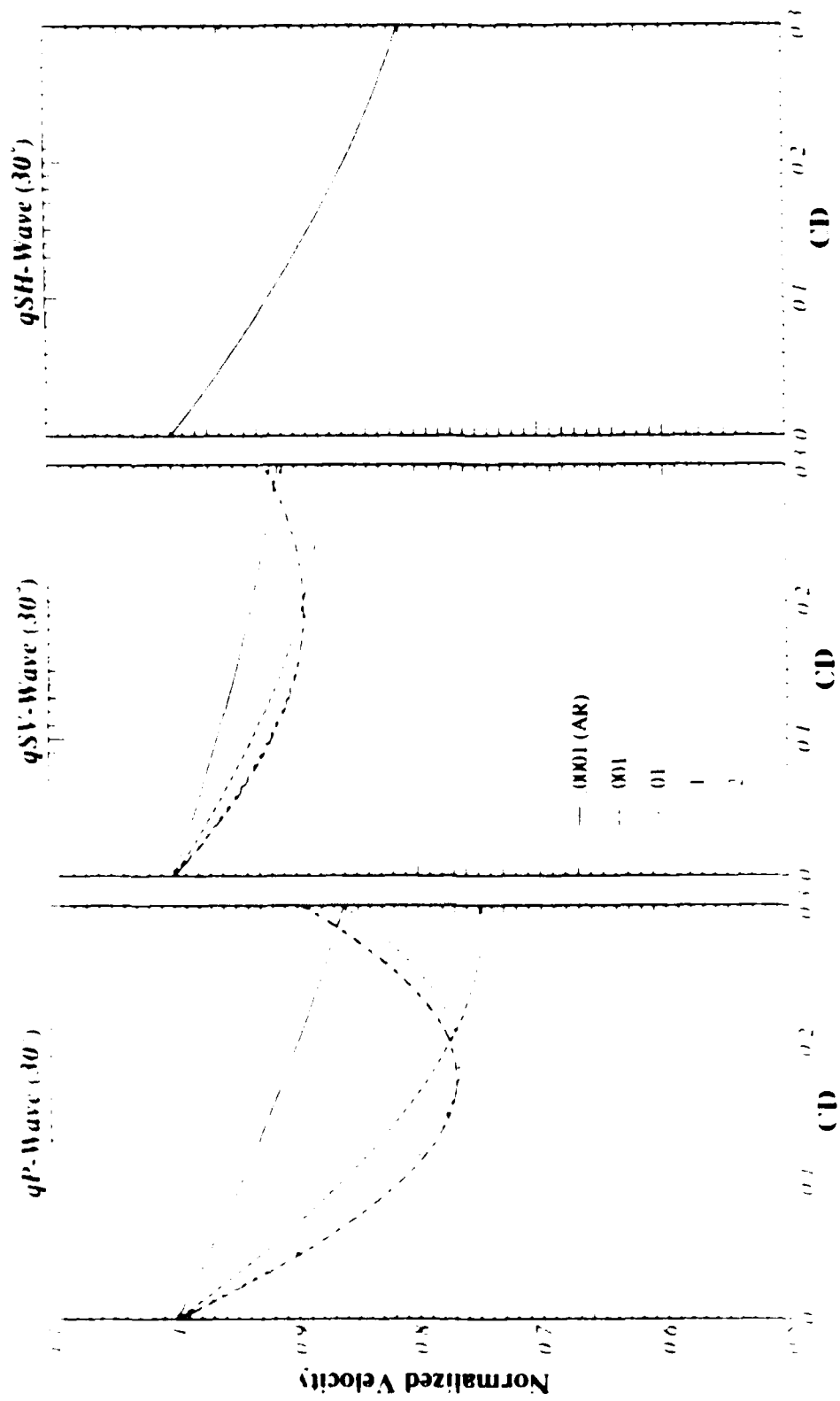


Figure 3b. Normalized velocity as a function of crack density and the aspect ratio for the wave incidence at 30° perpendicular to the crack plane including the second order theory.

Macro-fracture Model

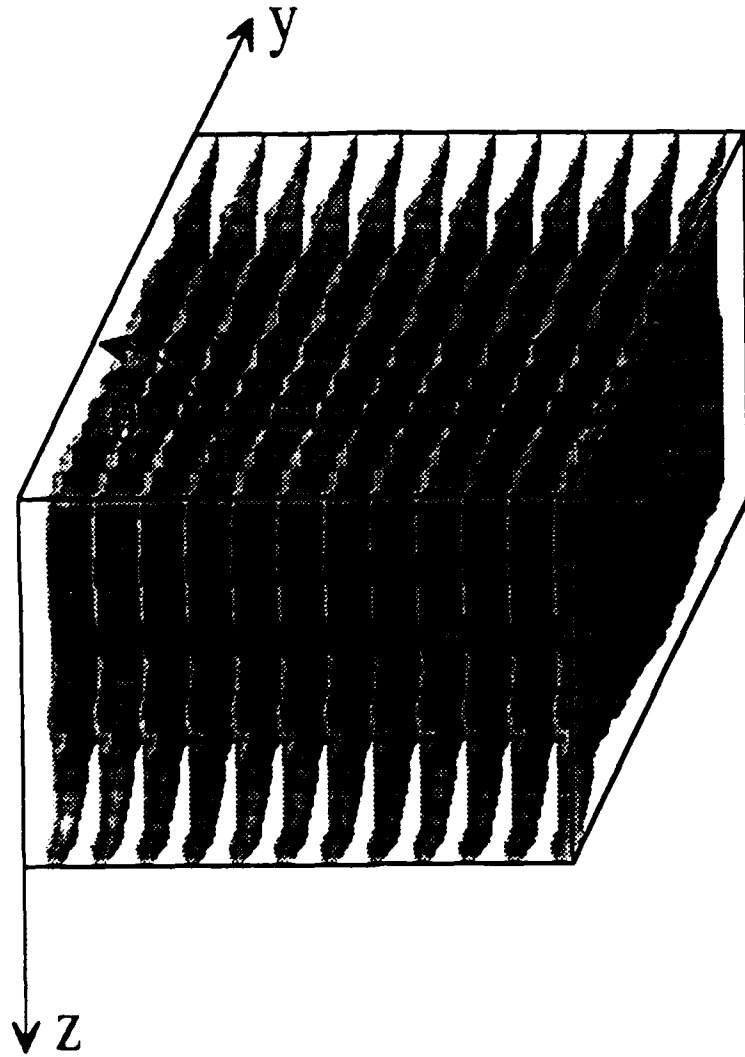


Figure 1. Schematic diagram of the macro fracture model. The r axis is the symmetry axis and is perpendicular to the fracture plane.

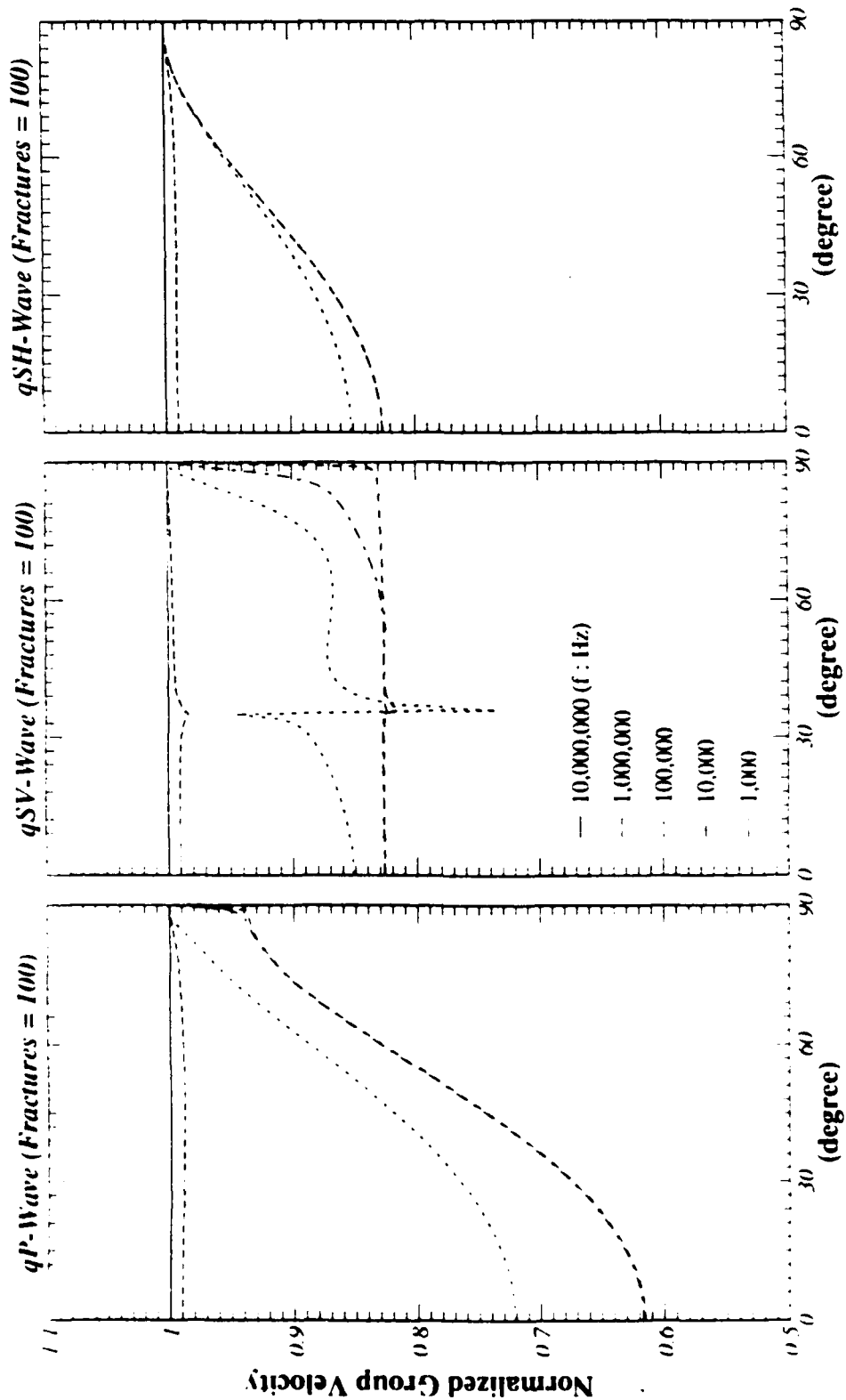


Figure 5: Azimuthal variation of normalized effective group velocity with change of frequency for specific stiffness (SS) 5.0×10^{12} Pa/m and for a rock mass with 100 fractures per meter. The nonfracture rock velocities are 5.0 (Vp) and 2.9 km/sec (Vs).

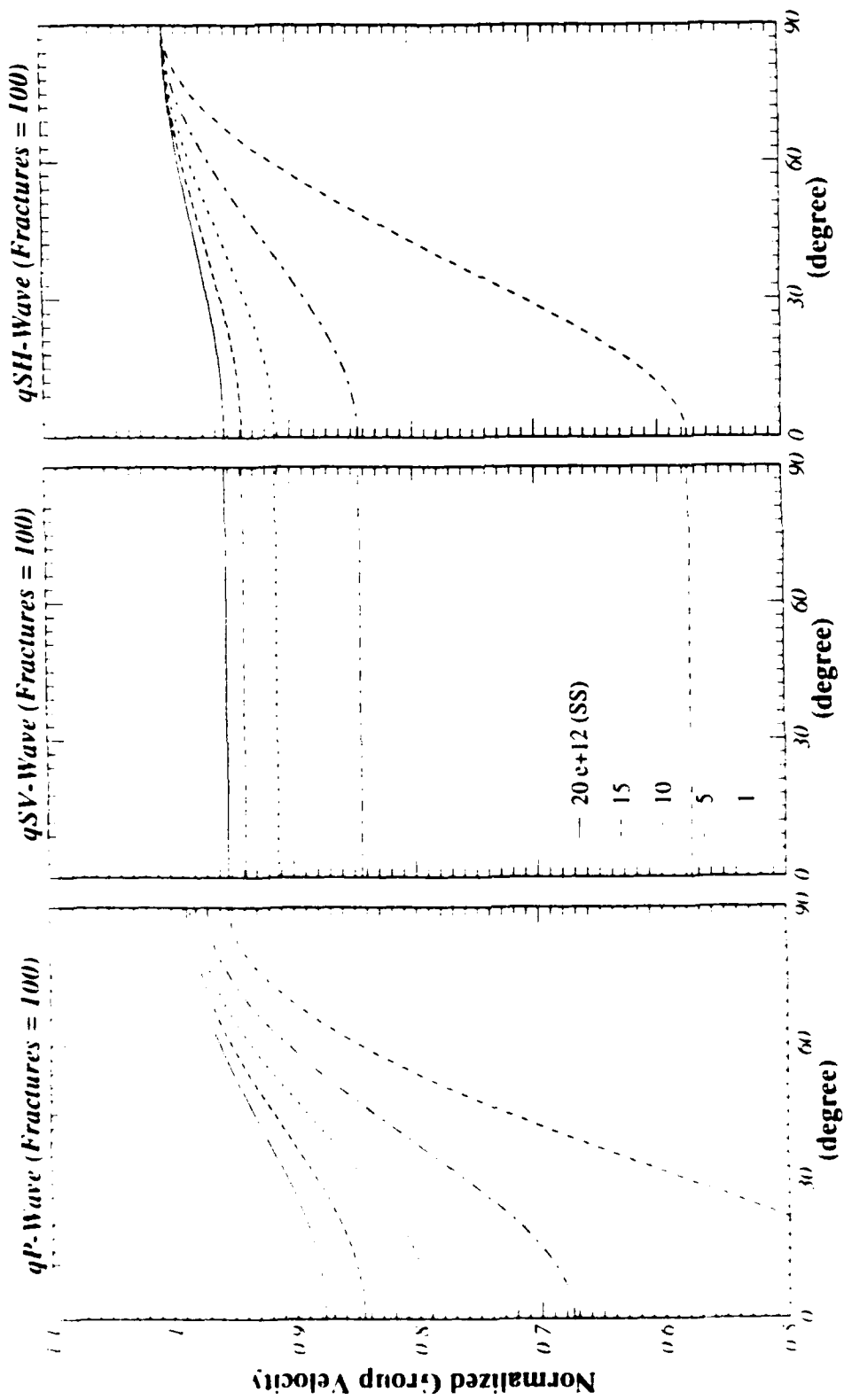


Figure 6: Azimuthal variation of normalized effective group velocity with change of specific stiffness (SS in Pa/m) for a rock mass with 100 fractures per meter using Schoenberg's average strain effective moduli.

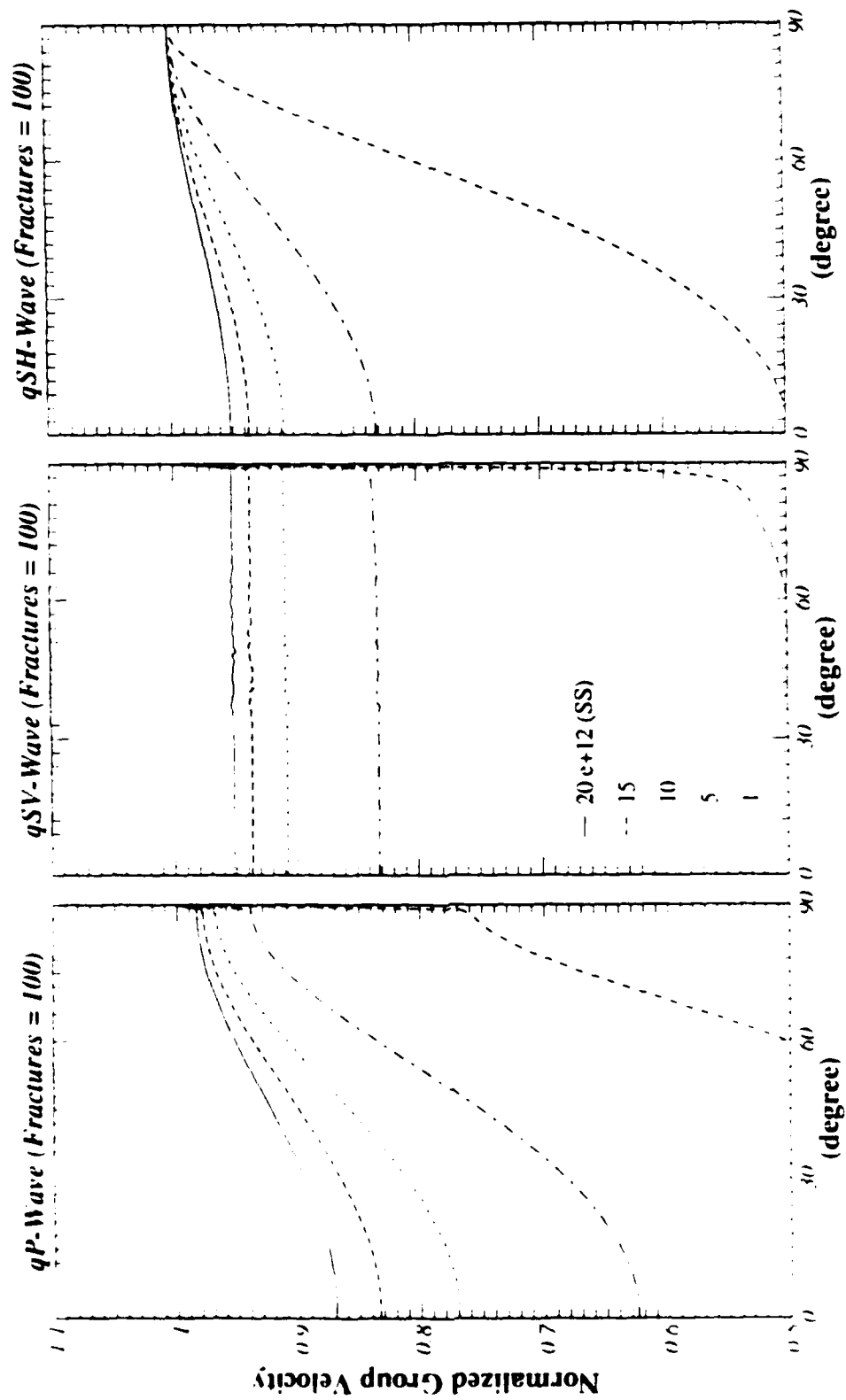


Figure 7: Azimuthal variation of normalized effective group velocity with change of specific stiffness (SS in Pa/m) for a rock mass with 100 fractures per meter using the displacement discontinuity fracture model.

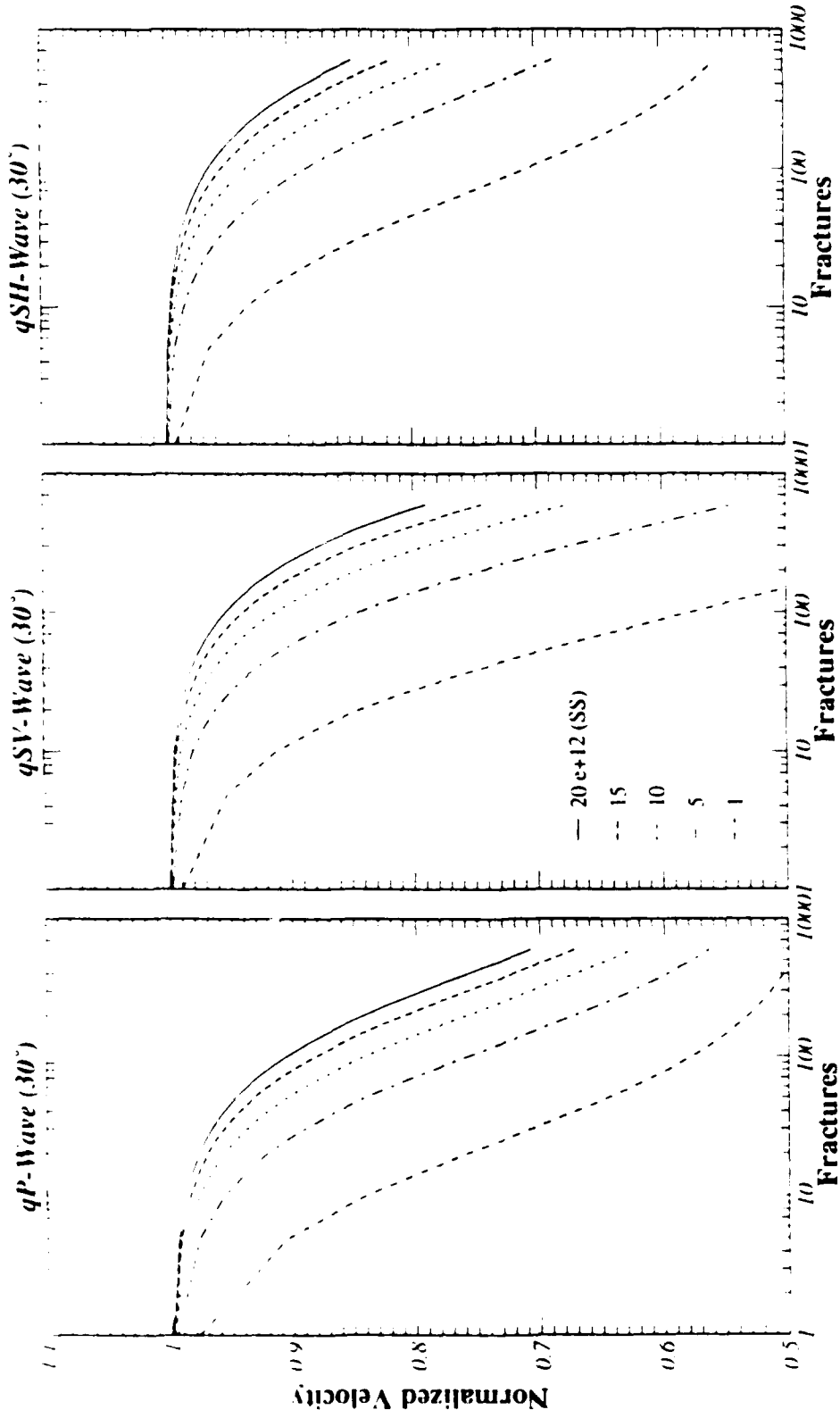


Figure 8: Normalized effective group velocity as a function of number of fractures per unit length and specific stiffness for the wave incidence at 30° from the perpendicular of the fracture plane.

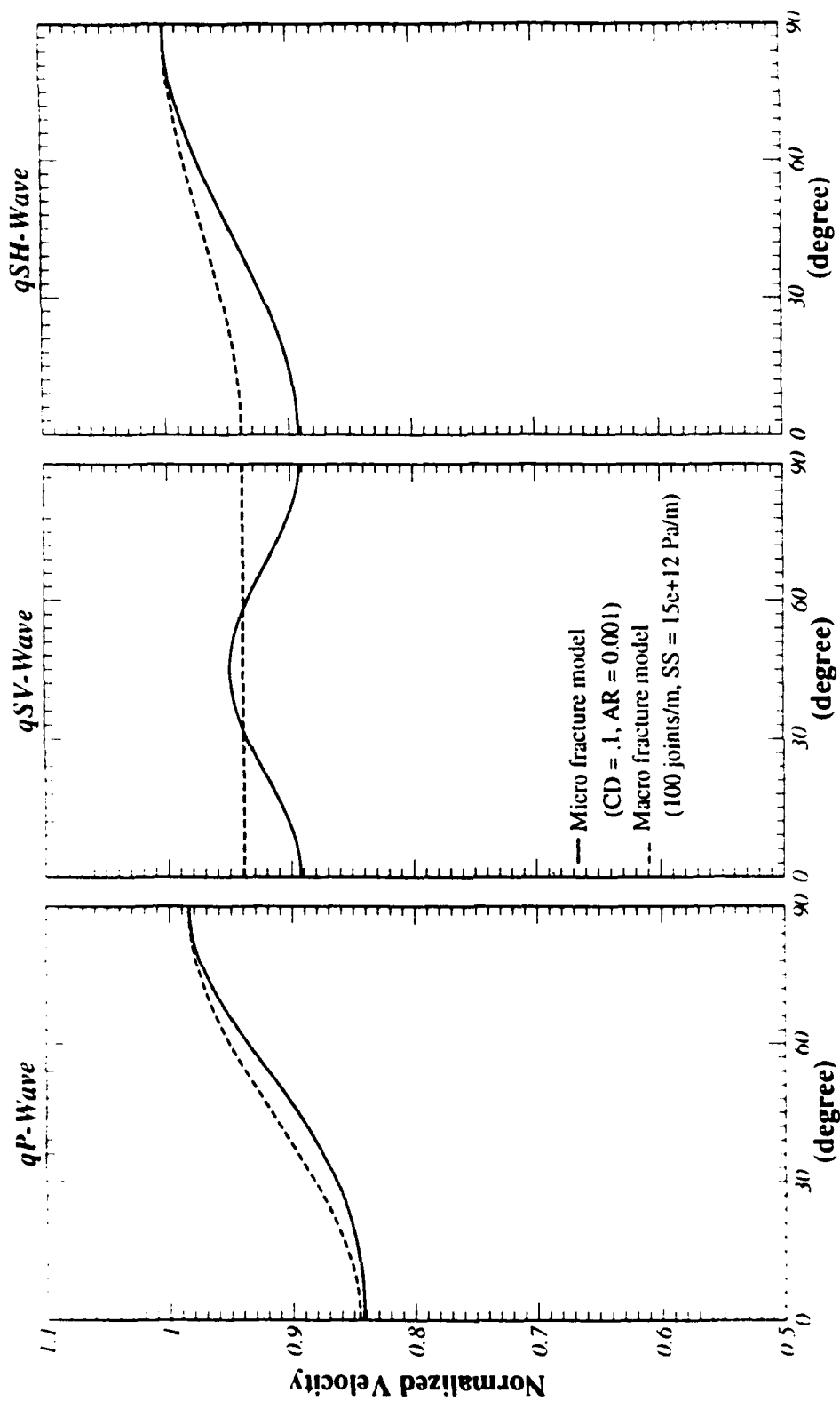


Figure 9: Comparison between two fracture models. Parameters of the medium and the model are shown. The two models were chosen to give a similar variation of the qP velocity.

Prof. Thomas Ahrens
Seismological Lab, 252-21
Division of Geological & Planetary Sciences
California Institute of Technology
Pasadena, CA 91125

Prof. Keiiti Aki
Center for Earth Sciences
University of Southern California
University Park
Los Angeles, CA 90089-0741

Prof. Shelton Alexander
Geosciences Department
403 Deike Building
The Pennsylvania State University
University Park, PA 16802

Dr. Ralph Alewine, III
DARPA/NMRO
3701 North Fairfax Drive
Arlington, VA 22203-1714

Prof. Charles B. Archambeau
CIRES
University of Colorado
Boulder, CO 80309

Dr. Thomas C. Bache, Jr.
Science Applications Int'l Corp.
10260 Campus Point Drive
San Diego, CA 92121 (2 copies)

Prof. Muawia Barazangi
Institute for the Study of the Continent
Cornell University
Ithaca, NY 14853

Dr. Jeff Barker
Department of Geological Sciences
State University of New York
at Binghamton
Vestal, NY 13901

Dr. Douglas R. Baumgardt
ENSCO, Inc
5400 Port Royal Road
Springfield, VA 22151-2388

Dr. Susan Beck
Department of Geosciences
Building #77
University of Arizona
Tuscon, AZ 85721

Dr. T.J. Bennett
S-CUBED
A Division of Maxwell Laboratories
11800 Sunrise Valley Drive, Suite 1212
Reston, VA 22091

Dr. Robert Blandford
AFTAC/TT, Center for Seismic Studies
1300 North 17th Street
Suite 1450
Arlington, VA 22209-2308

Dr. Stephen Bratt
Center for Seismic Studies
1300 North 17th Street
Suite 1450
Arlington, VA 22209-2308

Dr. Lawrence Burdick
IGPP, A-025
Scripps Institute of Oceanography
University of California, San Diego
La Jolla, CA 92093

Dr. Robert Burrige
Schlumberger-Doll Research Center
Old Quarry Road
Ridgefield, CT 06877

Dr. Jerry Carter
Center for Seismic Studies
1300 North 17th Street
Suite 1450
Arlington, VA 22209-2308

Dr. Eric Chael
Division 9241
Sandia Laboratory
Albuquerque, NM 87185

Dr. Martin Chapman
Department of Geological Sciences
Virginia Polytechnical Institute
21044 Derring Hall
Blacksburg, VA 24061

Prof. Vernon F. Cormier
Department of Geology & Geophysics
U-45, Room 207
University of Connecticut
Storrs, CT 06268

Prof. Steven Day
Department of Geological Sciences
San Diego State University
San Diego, CA 92182

Marvin Denny
U.S. Department of Energy
Office of Arms Control
Washington, DC 20585

Dr. Cliff Frolich
Institute of Geophysics
8701 North Mopac
Austin, TX 78759

Dr. Zoltan Der
ENSCO, Inc.
5400 Port Royal Road
Springfield, VA 22151-2388

Dr. Holly Given
IGPP, A-025
Scripps Institute of Oceanography
University of California, San Diego
La Jolla, CA 92093

Prof. Adam Dziewonski
Hoffman Laboratory, Harvard University
Dept. of Earth Atmos. & Planetary Sciences
20 Oxford Street
Cambridge, MA 02138

Dr. Jeffrey W. Given
SAIC
10260 Campus Point Drive
San Diego, CA 92121

Prof. John Ebel
Department of Geology & Geophysics
Boston College
Chestnut Hill, MA 02167

Dr. Dale Glover
Defense Intelligence Agency
ATTN: ODT-1B
Washington, DC 20301

Eric Fielding
SNEE Hall
INSTOC
Cornell University
Ithaca, NY 14853

Dr. Indra Gupta
Teledyne Geotech
314 Montgomery Street
Alexandria, VA 22314

Dr. Mark D. Fisk
Mission Research Corporation
735 State Street
P.O. Drawer 719
Santa Barbara, CA 93102

Dan N. Hagedon
Pacific Northwest Laboratories
Battelle Boulevard
Richland, WA 99352

Prof Stanley Flatte
Applied Sciences Building
University of California, Santa Cruz
Santa Cruz, CA 95064

Dr. James Hannon
Lawrence Livermore National Laboratory
P.O. Box 808
L-205
Livermore, CA 94550

Dr. John Foley
NER-Geo Sciences
1100 Crown Colony Drive
Quincy, MA 02169

Dr. Roger Hansen
HQ AFTAC/TTR
130 South Highway A1A
Patrick AFB, FL 32925-3002

Prof. Donald Forsyth
Department of Geological Sciences
Brown University
Providence, RI 02912

Prof. David G. Harkrider
Seismological Laboratory
Division of Geological & Planetary Sciences
California Institute of Technology
Pasadena, CA 91125

Dr. Art Frankel
U.S. Geological Survey
922 National Center
Reston, VA 22092

Prof. Danny Harvey
CIRES
University of Colorado
Boulder, CO 80309

Prof. Donald V. Helmberger
Seismological Laboratory
Division of Geological & Planetary Sciences
California Institute of Technology
Pasadena, CA 91125

Prof. Eugene Herrin
Institute for the Study of Earth and Man
Geophysical Laboratory
Southern Methodist University
Dallas, TX 75275

Prof. Robert B. Herrmann
Department of Earth & Atmospheric Sciences
St. Louis University
St. Louis, MO 63156

Prof. Lane R. Johnson
Seismographic Station
University of California
Berkeley, CA 94720

Prof. Thomas H. Jordan
Department of Earth, Atmospheric &
Planetary Sciences
Massachusetts Institute of Technology
Cambridge, MA 02139

Prof. Alan Kafka
Department of Geology & Geophysics
Boston College
Chestnut Hill, MA 02167

Robert C. Kemerait
ENSCO, Inc.
445 Pineda Court
Melbourne, FL 32940

Dr. Karl Koch
Institute for the Study of Earth and Man
Geophysical Laboratory
Southern Methodist University
Dallas, Tx 75275

Dr. Max Koontz
U.S. Dept. of Energy/DP 5
Forrestal Building
1000 Independence Avenue
Washington, DC 20585

Dr. Richard LaCoss
MIT Lincoln Laboratory, M-200B
P.O. Box 73
Lexington, MA 02173-0073

Dr. Fred K. Lamb
University of Illinois at Urbana-Champaign
Department of Physics
1110 West Green Street
Urbana, IL 61801

Prof. Charles A. Langston
Geosciences Department
403 Deike Building
The Pennsylvania State University
University Park, PA 16802

Jim Lawson, Chief Geophysicist
Oklahoma Geological Survey
Oklahoma Geophysical Observatory
P.O. Box 8
Leonard, OK 74043-0008

Prof. Thorne Lay
Institute of Tectonics
Earth Science Board
University of California, Santa Cruz
Santa Cruz, CA 95064

Dr. William Leith
U.S. Geological Survey
Mail Stop 928
Reston, VA 22092

Mr. James F. Lewkowicz
Phillips Laboratory/GPEH
29 Randolph Road
Hanscom AFB, MA 01731-3010(2 copies)

Mr. Alfred Lieberman
ACDA/VI-OA State Department Building
Room 5726
320-21st Street, NW
Washington, DC 20451

Prof. L. Timothy Long
School of Geophysical Sciences
Georgia Institute of Technology
Atlanta, GA 30332

Dr. Randolph Martin, III
New England Research, Inc.
76 Olcott Drive
White River Junction, VT 05001

Dr. Robert Masse
Denver Federal Building
Box 25046, Mail Stop 967
Denver, CO 80225

Dr. Gary McCartor
Department of Physics
Southern Methodist University
Dallas, TX 75275

Prof. Thomas V. McEvelly
Seismographic Station
University of California
Berkeley, CA 94720

Dr. Art McGarr
U.S. Geological Survey
Mail Stop 977
U.S. Geological Survey
Menlo Park, CA 94025

Dr. Keith L. McLaughlin
S-CUBED
A Division of Maxwell Laboratory
P.O. Box 1620
La Jolla, CA 92038-1620

Stephen Miller & Dr. Alexander Florence
SRI International
333 Ravenswood Avenue
Box AF 116
Menlo Park, CA 94025-3493

Prof. Bernard Minster
IGPP, A-025
Scripps Institute of Oceanography
University of California, San Diego
La Jolla, CA 92093

Prof. Brian J. Mitchell
Department of Earth & Atmospheric Sciences
St. Louis University
St. Louis, MO 63156

Mr. Jack Murphy
S-CUBED
A Division of Maxwell Laboratory
11800 Sunrise Valley Drive, Suite 1212
Reston, VA 22091 (2 Copies)

Dr. Keith K. Nakanishi
Lawrence Livermore National Laboratory
L-025
P.O. Box 808
Livermore, CA 94550

Dr. Carl Newton
Los Alamos National Laboratory
P.O. Box 1663
Mail Stop C335, Group ESS-3
Los Alamos, NM 87545

Dr. Bao Nguyen
HQ AFTAC/TTR
130 South Highway A1A
Patrick AFB, FL 32925-3002

Prof. John A. Orcutt
IGPP, A-025
Scripps Institute of Oceanography
University of California, San Diego
La Jolla, CA 92093

Prof. Jeffrey Park
Kline Geology Laboratory
P.O. Box 6666
New Haven, CT 06511-8130

Dr. Howard Patton
Lawrence Livermore National Laboratory
L-025
P.O. Box 808
Livermore, CA 94550

Dr. Frank Pilotte
HQ AFTAC/TT
130 South Highway A1A
Patrick AFB, FL 32925-3002

Dr. Jay J. Pulli
Radix Systems, Inc.
201 Perry Parkway
Gaithersburg, MD 20877

Dr. Robert Reinke
ATTN: FCTVTD
Field Command
Defense Nuclear Agency
Kirtland AFB, NM 87115

Prof. Paul G. Richards
Lamont-Doherty Geological Observatory
of Columbia University
Palisades, NY 10964

Mr. Wilmer Rivers
Teledyne Geotech
314 Montgomery Street
Alexandria, VA 22314

Dr. George Rothe
HQ AFTAC/TTR
130 South Highway A1A
Patrick AFB, FL 32925-3002

Dr. Alan S. Ryall, Jr.
DARPA/NMRO
3701 North Fairfax Drive
Arlington, VA 22209-1714

Dr. Richard Sailor
TASC, Inc.
55 Walkers Brook Drive
Reading, MA 01867

Prof. Charles G. Sammis
Center for Earth Sciences
University of Southern California
University Park
Los Angeles, CA 90089-0741

Prof. Christopher H. Scholz
Lamont-Doherty Geological Observatory
of Columbia University
Palisades, NY 10964

Dr. Susan Schwartz
Institute of Tectonics
1156 High Street
Santa Cruz, CA 95064

Secretary of the Air Force
(SAFRD)
Washington, DC 20330

Office of the Secretary of Defense
DDR&E
Washington, DC 20330

Thomas J. Sereno, Jr.
Science Application Int'l Corp.
10260 Campus Point Drive
San Diego, CA 92121

Dr. Michael Shore
Defense Nuclear Agency/SPSS
6801 Telegraph Road
Alexandria, VA 22310

Dr. Robert Shumway
University of California Davis
Division of Statistics
Davis, CA 95616

Dr. Matthew Sibol
Virginia Tech
Seismological Observatory
4044 Derring Hall
Blacksburg, VA 24061-0420

Prof. David G. Simpson
IRIS, Inc.
1616 North Fort Myer Drive
Suite 1050
Arlington, VA 22209

Donald L. Springer
Lawrence Livermore National Laboratory
L-025
P.O. Box 808
Livermore, CA 94550

Dr. Jeffrey Stevens
S-CUBED
A Division of Maxwell Laboratory
P.O. Box 1620
La Jolla, CA 92038-1620

Lt. Col. Jim Stobie
ATTN: AFOSR/NL
110 Duncan Avenue
Bolling AFB
Washington, DC 20332-0001

Prof. Brian Stump
Institute for the Study of Earth & Man
Geophysical Laboratory
Southern Methodist University
Dallas, TX 75275

Prof. Jeremiah Sullivan
University of Illinois at Urbana-Champaign
Department of Physics
1110 West Green Street
Urbana, IL 61801

Prof. L. Sykes
Lamont-Doherty Geological Observatory
of Columbia University
Palisades, NY 10964

Dr. David Taylor
ENSCO, Inc.
445 Pineda Court
Melbourne, FL 32940

Dr. Steven R. Taylor
Los Alamos National Laboratory
P.O. Box 1663
Mail Stop C335
Los Alamos, NM 87545

Prof. Clifford Thurber
University of Wisconsin-Madison
Department of Geology & Geophysics
1215 West Dayton Street
Madison, WI 53706

Prof. M. Nafi Toksoz
Earth Resources Lab
Massachusetts Institute of Technology
42 Carleton Street
Cambridge, MA 02142

Dr. Larry Turnbull
CIA-OSWR/NED
Washington, DC 20505

Dr. Gregory van der Vink
IRIS, Inc.
1616 North Fort Myer Drive
Suite 1050
Arlington, VA 22209

Dr. Karl Veith
EG&G
5211 Auth Road
Suite 240
Suitland, MD 20746

Prof. Terry C. Wallace
Department of Geosciences
Building #77
University of Arizona
Tucson, AZ 85721

Dr. Thomas Weaver
Los Alamos National Laboratory
P.O. Box 1663
Mail Stop C335
Los Alamos, NM 87545

Dr. William Wortman
Mission Research Corporation
4560 Underbed Road
Suite 704
Newington, VA 22222

Dr. Francis J. W. ...
Department of Geological Sciences
State University of New York
at Binghamton
Binghamton, NY 13902

Dr. ...
...
...
...
...

DARPA/PM
3701 North Fairfax Drive
Arlington, VA 22203-1714

DARPA/RMO/RETRIEVAL
3701 North Fairfax Drive
Arlington, VA 22203-1714

DARPA/RMO/SECURITY OFFICE
3701 North Fairfax Drive
Arlington, VA 22203-1714

HQ DNA
ATTN: Technical Library
Washington, DC 20305

Defense Intelligence Agency
Directorate for Scientific & Technical Intelligence
ATTN: DTIB
Washington, DC 20340-6158

Defense Technical Information Center
Cameron Station
Alexandria, VA 22314 (2 Copies)

TACTEC
Battelle Memorial Institute
505 King Avenue
Columbus, OH 43201 (Final Report)

Phillips Laboratory
ATTN: XPG
29 Randolph Road
Hanscom AFB, MA 01731-3010

Phillips Laboratory
ATTN: GPE
29 Randolph Road
Hanscom AFB, MA 01731-3010

Phillips Laboratory
ATTN: TSML
5 Wright Street
Hanscom AFB, MA 01731-3010

Phillips Laboratory
ATTN: PL/SUL
3550 Aberdeen Ave SE
Kirtland, NM 87117-5776 (2 copies)

Dr. Svein Mykkeltveit
NTNT/NORSAR
P.O. Box 51
N-2007 Kjeller, NORWAY (3 Copies)

Dr. Michel Bouchon
I.R.I.G.M.-B.P. 68
38402 St. Martin D'Herès
Cedex, FRANCE

Prof. Keith Priestley
University of Cambridge
Bullard Labs, Dept. of Earth Sciences
Madingley Rise, Madingley Road
Cambridge CB3 0EZ, ENGLAND

Dr. Michel Campillo
Observatoire de Grenoble
I.R.I.G.M.-B.P. 53
38041 Grenoble, FRANCE

Dr. Jorg Schlittenhardt
Federal Institute for Geosciences & Nat'l Res.
Postfach 510153
D-3000 Hannover 51, GERMANY

Dr. Kin Yip Chun
Geophysics Division
Physics Department
University of Toronto
Ontario, CANADA

Dr. Johannes Schweitzer
Institute of Geophysics
Ruhr University/Bochum
P.O. Box 1102148
4360 Bochum 1, GERMANY

Prof. Hans-Peter Harjes
Institute for Geophysics
Ruhr University/Bochum
P.O. Box 102148
4630 Bochum 1, GERMANY

Trust & Verify
VERTIC
8 John Adam Street
London WC2N 6EZ, ENGLAND

Prof. Eystein Husebye
NTNF/NORSAR
P.O. Box 51
N-2007 Kjeller, NORWAY

David Jepsen
Acting Head, Nuclear Monitoring Section
Bureau of Mineral Resources
Geology and Geophysics
G.P.O. Box 378, Canberra, AUSTRALIA

Ms. Eva Johannisson
Senior Research Officer
FOA
S-172 90 Sundbyberg, SWEDEN

Dr. Peter Marshall
Procurement Executive
Ministry of Defense
Blacknest, Brimpton
Reading FG7-FRS, UNITED KINGDOM

Dr. Bernard Massinon, Dr. Pierre Mechler
Societe Radiomana
27 rue Claude Bernard
75005 Paris, FRANCE (2 Copies)